

Global analysis of three–flavour neutrino oscillations: synergies and tensions in the determination of θ_{23} , δ_{CP} , and the mass ordering

Ivan Esteban,^a M. C. Gonzalez-Garcia,^{a,b,c} Alvaro Hernandez-Cabezudo,^d Michele Maltoni,^e Thomas Schwetz^d

^a*Departament de Física Quàntica i Astrofísica and Institut de Ciències del Cosmos, Universitat de Barcelona, Diagonal 647, E-08028 Barcelona, Spain*

^b*Institució Catalana de Recerca i Estudis Avançats (ICREA), Pg. Lluís Companys 23, 08010 Barcelona, Spain.*

^c*C.N. Yang Institute for Theoretical Physics, State University of New York at Stony Brook, Stony Brook, NY 11794-3840, USA*

^d*Institut für Kernphysik, Karlsruher Institut für Technologie (KIT), D-76021 Karlsruhe, Germany*

^e*Instituto de Física Teórica UAM/CSIC, Calle de Nicolás Cabrera 13–15, Universidad Autónoma de Madrid, Cantoblanco, E-28049 Madrid, Spain*

E-mail: ivan.esteban@fqa.ub.edu,
maria.gonzalez-garcia@stonybrook.edu, alvaro.cabezudo@kit.edu,
michele.maltoni@csic.es, schwetz@kit.edu

ABSTRACT: We present the results of a global analysis of the neutrino oscillation data available as of fall 2018 in the framework of three massive mixed neutrinos with the goal at determining the ranges of allowed values for the six relevant parameters. We describe the complementarity and quantify the tensions among the results of the different data samples contributing to the determination of each parameter. We also show how those vary when combining our global likelihood with the χ^2 map provided by Super-Kamiokande for their atmospheric neutrino data analysis in the same framework. The best fit of the analysis is for the normal mass ordering with inverted ordering being disfavoured with a $\Delta\chi^2 = 4.7$ (9.3) without (with) SK-atm. We find a preference for the second octant of θ_{23} , disfavoured the first octant with $\Delta\chi^2 = 4.4$ (6.0) without (with) SK-atm. The best fit for the complex phase is $\delta_{\text{CP}} = 215^\circ$ with CP conservation being allowed at $\Delta\chi^2 = 1.5$ (1.8). As a byproduct we quantify the correlated ranges for the laboratory observables sensitive to the absolute neutrino mass scale in beta decay, m_{ν_e} , and neutrino-less double beta decay, m_{ee} , and the total mass of the neutrinos, Σ , which is most relevant in Cosmology.

KEYWORDS: neutrino oscillations, solar and atmospheric neutrinos

Contents

1	Introduction	1
2	Global analysis: determination of oscillation parameters	2
2.1	Data samples analyzed	2
2.2	Summary of global fit results	3
3	Synergies and tensions	8
3.1	Status of comparison of results of solar experiments versus KamLAND	8
3.2	θ_{23} , δ_{CP} and mass ordering from LBL accelerator and MBL reactor experiments	10
3.2.1	Disappearance results and non-maximal θ_{23}	10
3.2.2	Appearance results, second θ_{23} octant and δ_{CP}	13
3.2.3	Preference for normal ordering	15
3.3	Treatment of atmospheric results from Super-Kamiokande and Deep-Core	18
4	Projections on neutrino mass scale observables	20
5	Conclusions	22
A	List of data used in the analysis	23
B	Technical details and validation cross checks	24
B.1	T2K	25
B.2	NOvA	25
B.3	Daya Bay	26
B.4	RENO	28

1 Introduction

Flavour transitions of neutrinos via the energy and distance dependent neutrino oscillation mechanism [1, 2] is a well established phenomenon, which proves that at least two out of the three neutrinos in the Standard Model must have tiny but non-zero masses. In this work we revisit the status of three-flavour neutrino oscillations in view of latest global data.

To fix the convention, the three flavour neutrinos, ν_e , ν_μ , ν_τ , are defined via the weak charged current. They are expressed as superposition of the three neutrino mass eigen-fields ν_i ($i = 1, 2, 3$) with masses m_i via a unitary leptonic mixing matrix [3, 4] by

$$\nu_\alpha = \sum_{i=1}^3 U_{\alpha i} \nu_i \quad (\alpha = e, \mu, \tau). \quad (1.1)$$

The mixing matrix we parametrize as:

$$U = \begin{pmatrix} 1 & 0 & 0 \\ 0 & c_{23} & s_{23} \\ 0 & -s_{23} & c_{23} \end{pmatrix} \cdot \begin{pmatrix} c_{13} & 0 & s_{13}e^{-i\delta_{\text{CP}}} \\ 0 & 1 & 0 \\ -s_{13}e^{i\delta_{\text{CP}}} & 0 & c_{13} \end{pmatrix} \cdot \begin{pmatrix} c_{21} & s_{12} & 0 \\ -s_{12} & c_{12} & 0 \\ 0 & 0 & 1 \end{pmatrix} \cdot \mathcal{P} \quad (1.2)$$

where $c_{ij} \equiv \cos \theta_{ij}$ and $s_{ij} \equiv \sin \theta_{ij}$. The angles θ_{ij} can be taken without loss of generality to lie in the first quadrant, $\theta_{ij} \in [0, \pi/2]$, and the phase $\delta_{\text{CP}} \in [0, 2\pi]$. Values of δ_{CP} different from 0 and π imply CP violation in neutrino oscillations in vacuum [5–7]. \mathcal{P} is a diagonal matrix which is the identity if neutrinos are Dirac fermions and it contains two additional phases, $\mathcal{P} = \text{diag}(e^{i\alpha_1}, e^{i\alpha_2}, 1)$, if they are Majorana fermions. The Majorana phases α_1 and α_2 play no role in neutrino oscillations [6, 8].

In this convention there are two non-equivalent orderings for the neutrino masses, namely normal ordering (NO) with $m_1 < m_2 < m_3$, and inverted ordering (IO) with $m_3 < m_1 < m_2$. Furthermore the data show a hierarchy between the mass splittings, $\Delta m_{21}^2 \ll |\Delta m_{31}^2| \simeq |\Delta m_{32}^2|$ with $\Delta m_{ij}^2 \equiv m_i^2 - m_j^2$. In this work we follow the convention from Ref. [9] and present our results for both, NO and IO, using the smallest and largest mass splittings. The smallest one is always Δm_{21}^2 , while the largest one we denote by $\Delta m_{3\ell}^2$, with $\ell = 1$ for NO and $\ell = 2$ for IO. Hence,

$$\Delta m_{3\ell}^2 = \begin{cases} \Delta m_{31}^2 > 0 & \text{for NO,} \\ \Delta m_{32}^2 < 0 & \text{for IO.} \end{cases} \quad (1.3)$$

Due to the wealth of experiments exploring neutrino oscillations, we are in the situation that a given parameter is determined by several measurements. Therefore, combined analyses such as the one presented below are an important tool to extract the full information on neutrino oscillation parameters. This is especially true for open questions, such as the octant of θ_{23} , the type of the neutrino mass ordering, and the status of the complex phase δ_{CP} , where some hints are emerging due to significant synergies between different experiments. However, also for parameters describing dominant oscillations, a significantly more accurate determination emerges by the combination of complementary data sets, such as for example for $|\Delta m_{3\ell}^2|$.

We present below the global fit NuFIT-4.0, updating our previous analyses [9–11]. $\Delta\chi^2$ maps and future updates of this analysis will be made available at the NuFIT website [12]. For other recent global fits see [13, 14].

2 Global analysis: determination of oscillation parameters

2.1 Data samples analyzed

The analysis presented below uses data available up to fall 2018. A complete list of the used data including references can be found in appendix A. Here we give a brief overview of recent updates and mention changes with respect to our previous analysis [11].

We include latest data from the MINOS [15, 16], T2K [17, 18], and NOvA [19, 20] long-baseline accelerator experiments from ν_μ disappearance and $\nu_\mu \rightarrow \nu_e$ appearance

channels, both for neutrino and anti-neutrino beam modes. In particular, T2K and NOvA have presented updated results at the Neutrino18 conference, including also first data on anti-neutrinos from NOvA, whose impact will be discussed below.

Concerning reactor neutrino experiments, the fit of data with baselines in the km range (medium baseline, MBL) is completely dominated by modern experiments, most importantly by Daya Bay [21], with subleading contributions from RENO [22] and Double Chooz [23]. Moreover, those experiments are entirely based on relative spectra from detectors at different baselines, and are therefore largely independent of reactor neutrino flux predictions. In view of the unclear situation of reactor flux predictions and reactor data at very short baselines (see, *e.g.*, Ref. [24] for a recent discussion), we decided to include only the modern MBL reactor experiments Daya Bay, RENO, and Double Chooz. For the analysis of KamLAND long-baseline reactor data we replaced predicted neutrino fluxes by the spectrum measured in Daya Bay near detectors [25], which makes also our KamLAND analysis largely independent of flux predictions.

Our solar neutrino data includes previous data from radio-chemical and the SNO experiments, as well as updated exposures from Super-Kamiokande and Borexino, see appendix A for the detailed list and references.¹

Atmospheric neutrino data generically are difficult to analyze outside the experimental collaborations. We present below two separate global analyses, depending on the used atmospheric neutrino data. Our default analysis makes use of IceCube/DeepCore 3-year data [27] which can be re-analyzed using the information provided by the collaboration [28]. Especially in the context of the mass ordering determination, atmospheric neutrino data from Super-Kamiokande 1-4 [29] seems to provide important information. Unfortunately there is not enough information available to reproduce these results outside the collaboration. However, Super-Kamiokande has published the results of their analysis in the form of a tabulated χ^2 map [30], which we can combine with our global analysis. We will show the results of this combination as an alternative global fit. A detailed discussion of atmospheric neutrino data, including also the potential impact of an alternative IceCube analysis [31] will be presented in section 3.3.

2.2 Summary of global fit results

The results of our global fit are displayed in fig. 1 (one-dimensional $\Delta\chi^2$ curves) and fig. 2 (two-dimensional projections of confidence regions). In table 1 we give the best fit values as well as 1σ and 3σ confidence intervals for the oscillation parameters. We show two versions of the results. The default analysis is without Super-Kamiokande atmospheric neutrino data (SK-atm), and contains all the data for which a fit can be performed. For the alternative analysis, we add the pre-calculated $\Delta\chi^2$ table from SK-atm provided by the collaboration to our global fit, in order to illustrate the potential impact of these data. Let us summarize here the main features of the global fit result. More detailed discussions about how certain features emerge will be given in the following sections.

¹We do not include here the latest data release from Borexino [26], which is expected to have a very small impact on the determination of oscillation parameters. These data will be included in future updates of our global fit.

		Normal Ordering (best fit)		Inverted Ordering ($\Delta\chi^2 = 4.7$)	
		bfp $\pm 1\sigma$	3σ range	bfp $\pm 1\sigma$	3σ range
without SK-atm	$\sin^2 \theta_{12}$	$0.310^{+0.013}_{-0.012}$	$0.275 \rightarrow 0.350$	$0.310^{+0.013}_{-0.012}$	$0.275 \rightarrow 0.350$
	$\theta_{12}/^\circ$	$33.82^{+0.78}_{-0.76}$	$31.61 \rightarrow 36.27$	$33.82^{+0.78}_{-0.76}$	$31.61 \rightarrow 36.27$
	$\sin^2 \theta_{23}$	$0.580^{+0.017}_{-0.021}$	$0.418 \rightarrow 0.627$	$0.584^{+0.016}_{-0.020}$	$0.423 \rightarrow 0.629$
	$\theta_{23}/^\circ$	$49.6^{+1.0}_{-1.2}$	$40.3 \rightarrow 52.4$	$49.8^{+1.0}_{-1.1}$	$40.6 \rightarrow 52.5$
	$\sin^2 \theta_{13}$	$0.02241^{+0.00065}_{-0.00065}$	$0.02045 \rightarrow 0.02439$	$0.02264^{+0.00066}_{-0.00066}$	$0.02068 \rightarrow 0.02463$
	$\theta_{13}/^\circ$	$8.61^{+0.13}_{-0.13}$	$8.22 \rightarrow 8.99$	$8.65^{+0.13}_{-0.13}$	$8.27 \rightarrow 9.03$
	$\delta_{\text{CP}}/^\circ$	215^{+40}_{-29}	$125 \rightarrow 392$	284^{+27}_{-29}	$196 \rightarrow 360$
	$\frac{\Delta m_{21}^2}{10^{-5} \text{ eV}^2}$	$7.39^{+0.21}_{-0.20}$	$6.79 \rightarrow 8.01$	$7.39^{+0.21}_{-0.20}$	$6.79 \rightarrow 8.01$
$\frac{\Delta m_{3\ell}^2}{10^{-3} \text{ eV}^2}$	$+2.525^{+0.033}_{-0.032}$	$+2.427 \rightarrow +2.625$	$-2.512^{+0.034}_{-0.032}$	$-2.611 \rightarrow -2.412$	
		Normal Ordering (best fit)		Inverted Ordering ($\Delta\chi^2 = 9.3$)	
		bfp $\pm 1\sigma$	3σ range	bfp $\pm 1\sigma$	3σ range
with SK-atm	$\sin^2 \theta_{12}$	$0.310^{+0.013}_{-0.012}$	$0.275 \rightarrow 0.350$	$0.310^{+0.013}_{-0.012}$	$0.275 \rightarrow 0.350$
	$\theta_{12}/^\circ$	$33.82^{+0.78}_{-0.76}$	$31.61 \rightarrow 36.27$	$33.82^{+0.78}_{-0.75}$	$31.62 \rightarrow 36.27$
	$\sin^2 \theta_{23}$	$0.582^{+0.015}_{-0.019}$	$0.428 \rightarrow 0.624$	$0.582^{+0.015}_{-0.018}$	$0.433 \rightarrow 0.623$
	$\theta_{23}/^\circ$	$49.7^{+0.9}_{-1.1}$	$40.9 \rightarrow 52.2$	$49.7^{+0.9}_{-1.0}$	$41.2 \rightarrow 52.1$
	$\sin^2 \theta_{13}$	$0.02240^{+0.00065}_{-0.00066}$	$0.02044 \rightarrow 0.02437$	$0.02263^{+0.00065}_{-0.00066}$	$0.02067 \rightarrow 0.02461$
	$\theta_{13}/^\circ$	$8.61^{+0.12}_{-0.13}$	$8.22 \rightarrow 8.98$	$8.65^{+0.12}_{-0.13}$	$8.27 \rightarrow 9.03$
	$\delta_{\text{CP}}/^\circ$	217^{+40}_{-28}	$135 \rightarrow 366$	280^{+25}_{-28}	$196 \rightarrow 351$
	$\frac{\Delta m_{21}^2}{10^{-5} \text{ eV}^2}$	$7.39^{+0.21}_{-0.20}$	$6.79 \rightarrow 8.01$	$7.39^{+0.21}_{-0.20}$	$6.79 \rightarrow 8.01$
$\frac{\Delta m_{3\ell}^2}{10^{-3} \text{ eV}^2}$	$+2.525^{+0.033}_{-0.031}$	$+2.431 \rightarrow +2.622$	$-2.512^{+0.034}_{-0.031}$	$-2.606 \rightarrow -2.413$	

Table 1. Three-flavour oscillation parameters from our fit to global data. The numbers in the 1st (2nd) column are obtained assuming NO (IO), *i.e.*, relative to the respective local minimum. Note that $\Delta m_{3\ell}^2 \equiv \Delta m_{31}^2 > 0$ for NO and $\Delta m_{3\ell}^2 \equiv \Delta m_{32}^2 < 0$ for IO. The results shown in the upper (lower) table are without (with) adding the tabulated SK-atm $\Delta\chi^2$.

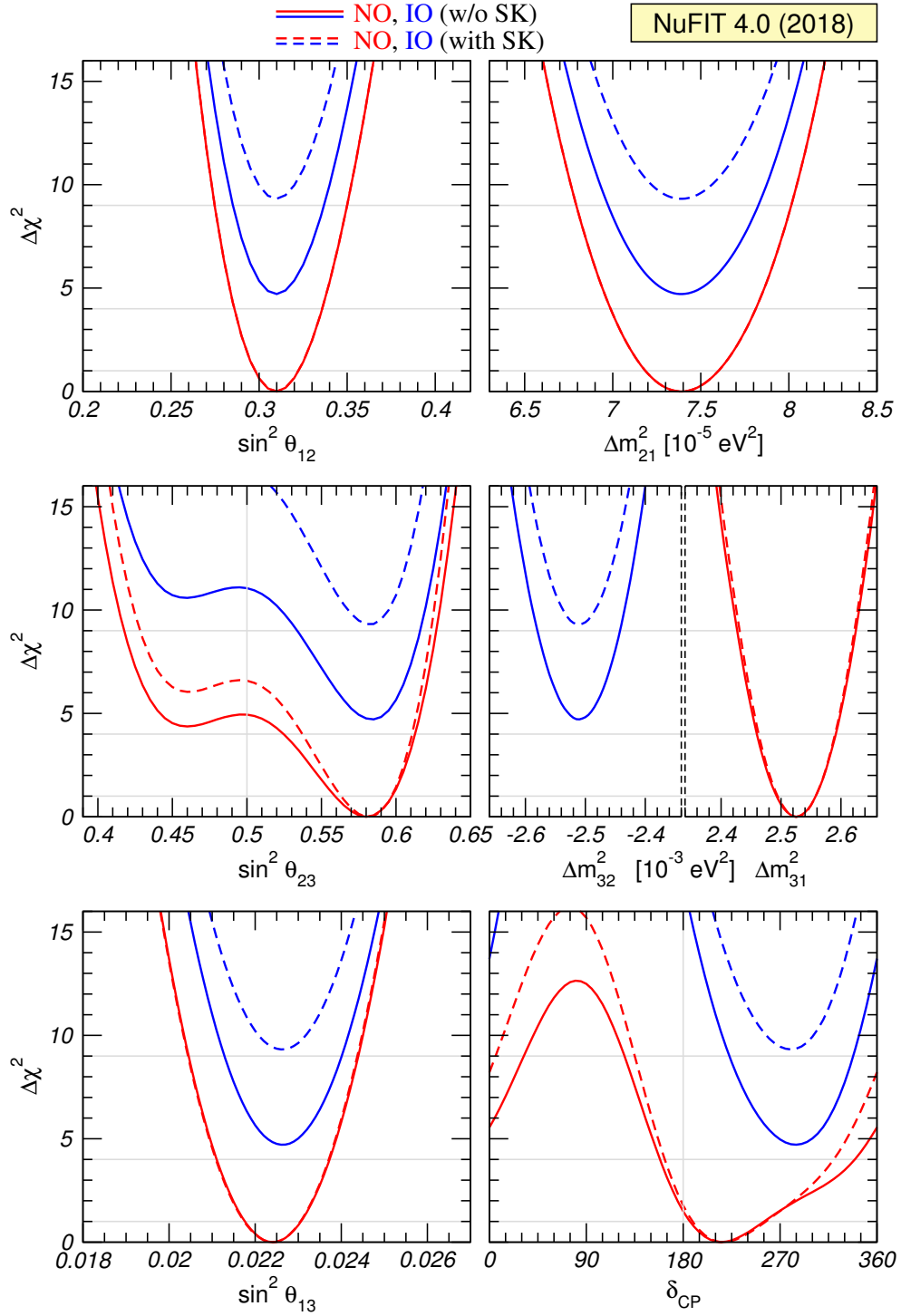


Figure 1. Global 3ν oscillation analysis. We show $\Delta\chi^2$ profiles minimized with respect to all undisplayed parameters. The red (blue) curves correspond to Normal (Inverted) Ordering. Solid (dashed) curves are without (with) adding the tabulated SK-atm $\Delta\chi^2$. Note that as atmospheric mass-squared splitting we use Δm_{31}^2 for NO and Δm_{32}^2 for IO.

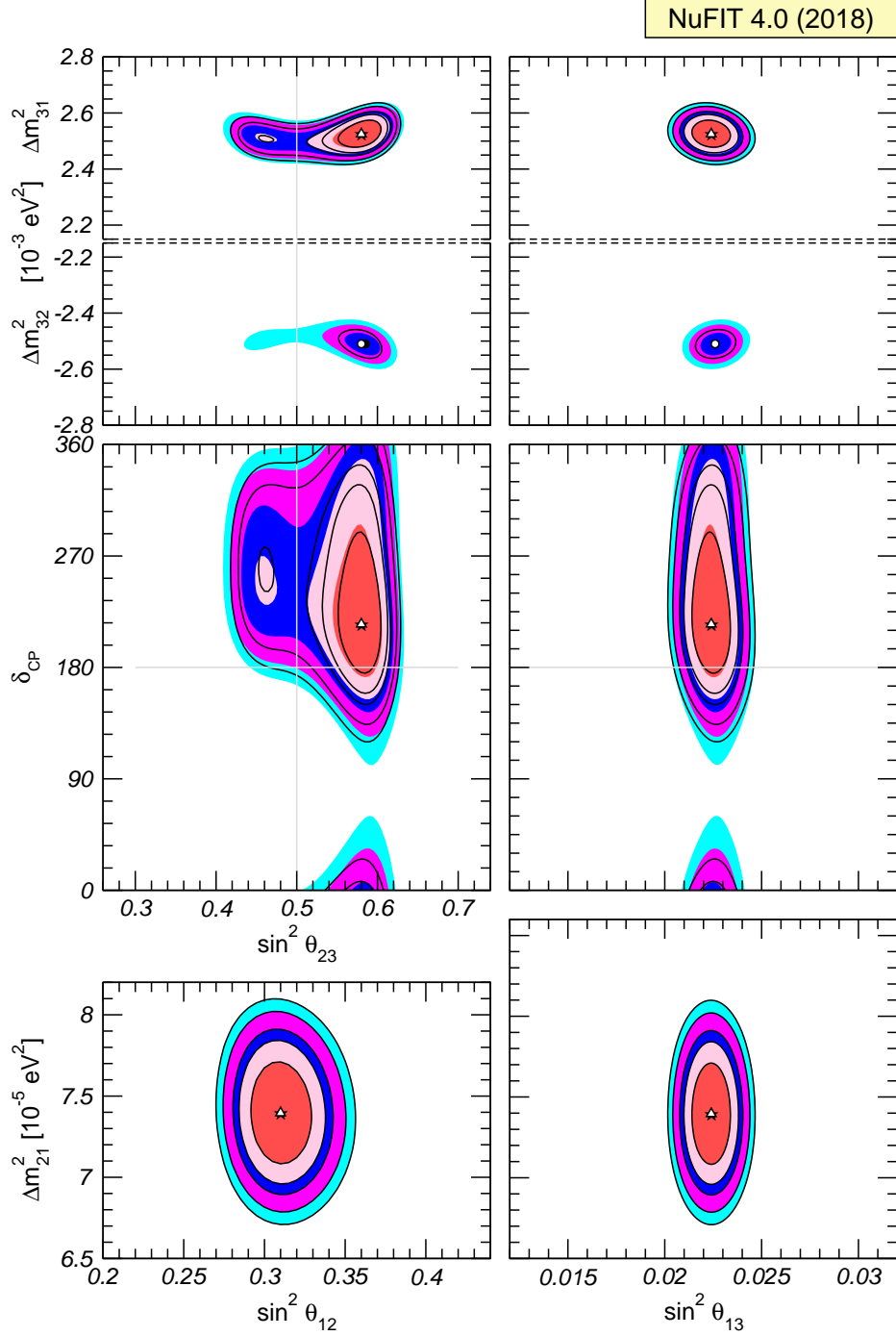


Figure 2. Global 3ν oscillation analysis. Each panel shows the two-dimensional projection of the allowed six-dimensional region after minimization with respect to the undisplayed parameters. The regions in the four lower panels are obtained from $\Delta\chi^2$ minimized with respect to the mass ordering. The different contours correspond to 1σ , 90%, 2σ , 99%, 3σ CL (2 dof). Coloured regions (black contour curves) are without (with) adding the tabulated SK-atm $\Delta\chi^2$. Note that as atmospheric mass-squared splitting we use Δm_{31}^2 for NO and Δm_{32}^2 for IO.

Except for $\sin^2 \theta_{23}$ and δ_{CP} the $\Delta\chi^2$ shapes are close to parabolic, indicating that the χ^2 approximation for the distribution should hold to good accuracy. The Monte Carlo studies performed in Refs. [11, 32] indicate that also for $\sin^2 \theta_{23}$, δ_{CP} and the mass ordering the χ^2 approximation gives a reasonable estimate of the corresponding confidence level. Therefore, the $\Delta\chi^2$ values given below can be converted into an approximate number of standard deviations by the $\sqrt{\Delta\chi^2}$ rule.

Defining the 3σ relative precision of the parameter by $2(x^{\text{up}} - x^{\text{low}})/(x^{\text{up}} + x^{\text{low}})$, where x^{up} (x^{low}) is the upper (lower) bound on a parameter x at the 3σ level, we obtain the following 3σ relative precisions (marginalizing over ordering):

$$\begin{aligned} 14\% (\theta_{12}) \quad , \quad 8.9\% (\theta_{13}) \quad , \quad 27 [24]\% (\theta_{23}) , \\ 16\% (\Delta m_{21}^2) , \quad 7.8 [7.6]\% (|\Delta m_{3\ell}^2|) , \quad 100 [92]\% (\delta_{\text{CP}}) , \end{aligned} \quad (2.1)$$

where the numbers between brackets show the impact of including SK-atm in the precision of that parameter determination. We notice that as $\Delta\chi^2$ shape for δ_{CP} is clearly not gaussian this evaluation of its ‘‘precision’’ can only be taken as indicative.

Altogether the status of mass ordering discrimination, determination of $\sin^2 \theta_{23}$, and the leptonic CP phase δ_{CP} can be summarized as follows:

- The best fit is for the normal mass ordering. Inverted ordering is disfavoured with a $\Delta\chi^2 = 4.7 (9.3)$ without (with) SKatm.
- We obtain preference for the second octant of θ_{23} , with the best fit point located at $\sin^2 \theta_{23} = 0.58$. Values with $\sin^2 \theta_{23} \leq 0.5$ are disfavoured with $\Delta\chi^2 = 4.4 (6.0)$ without (with) SK-atm.
- The best fit for the complex phase is at $\delta_{\text{CP}} = 215^\circ$. Compared to previous results (*e.g.*, NuFIT 3.2 [12]), the allowed range is pushed towards the CP conserving value of 180° , which now is only disfavoured with $\Delta\chi^2 = 1.5 (1.8)$ without (with) SK-atm.

In table 1 we give the best fit values and confidence intervals for both mass orderings, relative to the local best fit points in each ordering. The global confidence intervals (marginalizing also over the ordering) are identical to the ones for normal ordering, which have also been used in eq. (2.1). The only exception to this statement is $\Delta m_{3\ell}^2$ in the analysis without SK-atm; in this case a disconnected interval would appear above 2σ corresponding to negative values of $\Delta m_{3\ell}^2$ (*i.e.*, inverted ordering). Altogether we derive the following 3σ ranges on the magnitude of the elements of the leptonic mixing matrix:

$$\begin{aligned} |U|_{3\sigma}^{\text{w/o SK atm}} &= \begin{pmatrix} 0.797 \rightarrow 0.842 & 0.518 \rightarrow 0.585 & 0.143 \rightarrow 0.156 \\ 0.233 \rightarrow 0.495 & 0.448 \rightarrow 0.679 & 0.639 \rightarrow 0.783 \\ 0.287 \rightarrow 0.532 & 0.486 \rightarrow 0.706 & 0.604 \rightarrow 0.754 \end{pmatrix} \\ |U|_{3\sigma}^{\text{w SK atm}} &= \begin{pmatrix} 0.797 \rightarrow 0.842 & 0.518 \rightarrow 0.585 & 0.143 \rightarrow 0.156 \\ 0.235 \rightarrow 0.484 & 0.458 \rightarrow 0.671 & 0.647 \rightarrow 0.781 \\ 0.304 \rightarrow 0.531 & 0.497 \rightarrow 0.699 & 0.607 \rightarrow 0.747 \end{pmatrix} \end{aligned} \quad (2.2)$$

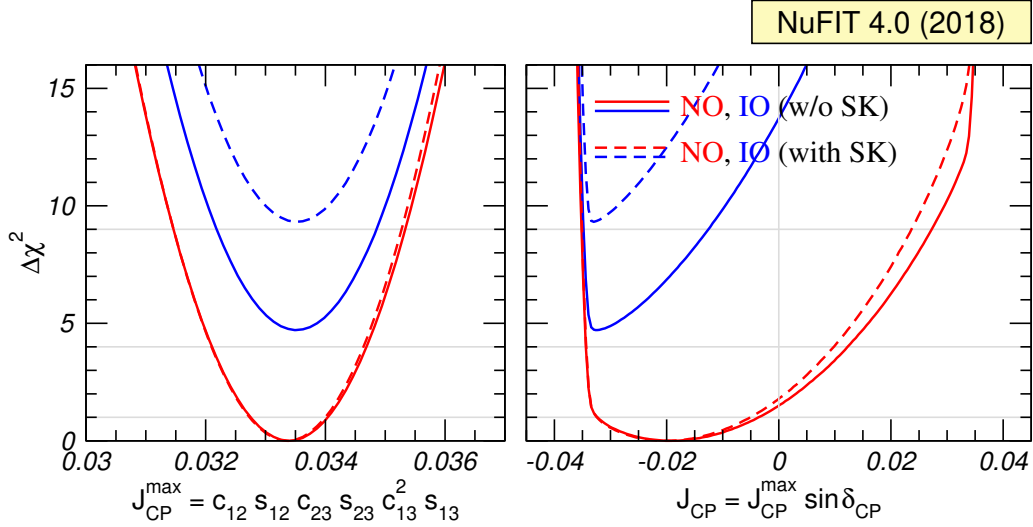


Figure 3. Dependence of the global $\Delta\chi^2$ function on the Jarlskog invariant. The red (blue) curves are for NO (IO). Solid (dashed) curves are without (with) adding the tabulated SK-atm $\Delta\chi^2$.

Note that there are strong correlations between the elements due to the unitary constraint, see Ref. [33] for details on how we derive the ranges.

The present status of leptonic CP violation is illustrated in figs. 2 and 3. In particular fig. 2 contains two projections of the confidence regions with δ_{CP} on the vertical axis in which we observe the non-trivial correlations between δ_{CP} and $\sin^2\theta_{23}$. In the left panel of fig. 3 we show the dependence of $\Delta\chi^2$ of the global analysis on the Jarlskog invariant which gives a convention-independent measure of CP violation [34], defined by:

$$\begin{aligned} J_{\text{CP}} &\equiv \text{Im} [U_{\alpha i} U_{\alpha j}^* U_{\beta i}^* U_{\beta j}] \\ &\equiv J_{\text{CP}}^{\text{max}} \sin \delta_{\text{CP}} = \cos \theta_{12} \sin \theta_{12} \cos \theta_{23} \sin \theta_{23} \cos^2 \theta_{13} \sin \theta_{13} \sin \delta_{\text{CP}} \end{aligned} \quad (2.3)$$

where in the second line we have used the parametrization in Eq. (1.2). Factoring out $\sin \delta_{\text{CP}}$, the determination of the mixing angles implies a maximal possible value of the Jarlskog invariant:

$$J_{\text{CP}}^{\text{max}} = 0.0333 \pm 0.0006 (\pm 0.0019) \quad (2.4)$$

at 1σ (3σ) for both orderings. The preference of the present data for non-zero δ_{CP} implies a best fit value $J_{\text{CP}}^{\text{best}} = -0.019$, which is favored over CP conservation with $\Delta\chi^2 = 1.5$ (1.8) without (with) SK-atm. These numbers can be compared with the size of the Jarlskog invariant in the quark sector, $J_{\text{CP}}^{\text{quarks}} = (3.18 \pm 0.15) \times 10^{-5}$ [35].

3 Synergies and tensions

3.1 Status of comparison of results of solar experiments versus KamLAND

The analyses of the solar experiments and of KamLAND give the dominant contribution to the determination of Δm_{21}^2 and θ_{12} . We show in fig. 4 the present determination of these

parameters from the global solar analysis in comparison with that of KamLAND data. The results of the solar neutrino analysis are shown for the two latest versions of the Standard Solar Model, namely the GS98 and the AGSS09 models [36] obtained with two different determinations of the solar abundances [37]. This clearly illustrates the independence of the results with respect to the solar modeling.

There are two main differences compared to our previous published results in Ref. [11]. In what respects the KamLAND region it has shifted towards slightly smaller values of θ_{12} . This effect arises mainly from the new reactor fluxes used in our analysis of the KamLAND data. As mentioned in section 2.1, in our calculation of the event rates in KamLAND we have replaced the predicted neutrino fluxes by the spectrum measured in Daya Bay near detectors [25] which is unfolded for detector and remaining oscillation effects. In Ref. [11] we used instead the unoscillated reactor determined by including in the fit the results from a compilation of short baseline reactor data. The net result is that the current unoscillated reactor fluxes are slightly lower and consequently a slightly higher survival probability is required to better fit the data. Since in the context of 3ν -oscillations

$$P_{ee, \text{KamLAND}}^{3\nu} = \sin^4 \theta_{13} + \cos^4 \theta_{13} \left(1 - \frac{1}{2} \sin^2(2\theta_{12}) \sin^2 \frac{\Delta m_{21}^2 L}{2E} \right) \quad (3.1)$$

a larger survival probability implies smaller values of θ_{12} . As a result the best-fit value of θ_{12} determined by KamLAND, $\sin^2 \theta_{12, \text{bf-Kam}} = 0.290$, does not perfectly align with the corresponding best fit value from the solar neutrino analysis, $\sin^2 \theta_{12, \text{bf-sol}} = 0.315$. Statistically, however, this is a very small effect as the best fit value of $\sin^2 \theta_{12} = 0.315$ lies at $\Delta\chi_{\text{KamLAND}}^2 \lesssim 1$.

In what respects the determination of Δm_{21}^2 it has been a result of global analyses for several years already, that the value of Δm_{21}^2 preferred by KamLAND is somewhat higher than the one from solar experiments. The tension arises from a combination of two effects: the well-known fact that none of the ${}^8\text{B}$ measurements performed by SNO, SK and Borexino shows any evidence of the low energy spectrum turn-up expected in the standard LMA-MSW [38, 39] solution for the value of Δm_{21}^2 favored by KamLAND; and the observation of a non-vanishing day-night asymmetry in SK, whose size is larger than the one predicted for the Δm_{21}^2 value indicated of KamLAND.

The new addition to this issue in the present analysis is the inclusion of the 2860-day energy spectrum of SK4 [40] (compared to the 2365-day energy spectrum used in [11]). For the day-night variation of the results we still use the SK4 2055-day day-night asymmetry [41] because SK has not presented any update concerning the day-night dependence of the observed rates. The inclusion of the new spectral data makes the lack of the turn-up effect slightly stronger (for example the best fit Δm_{21}^2 of KamLAND was at $\Delta\chi_{\text{solar}}^2 = 4$ in the analysis of [11] with the GS98 fluxes and it is now at $\Delta\chi_{\text{solar}}^2 = 4.7$). For illustration of the relevance of the day-night variation results we plot in fig. 4 the corresponding results of the solar analysis without including the day-night asymmetry.

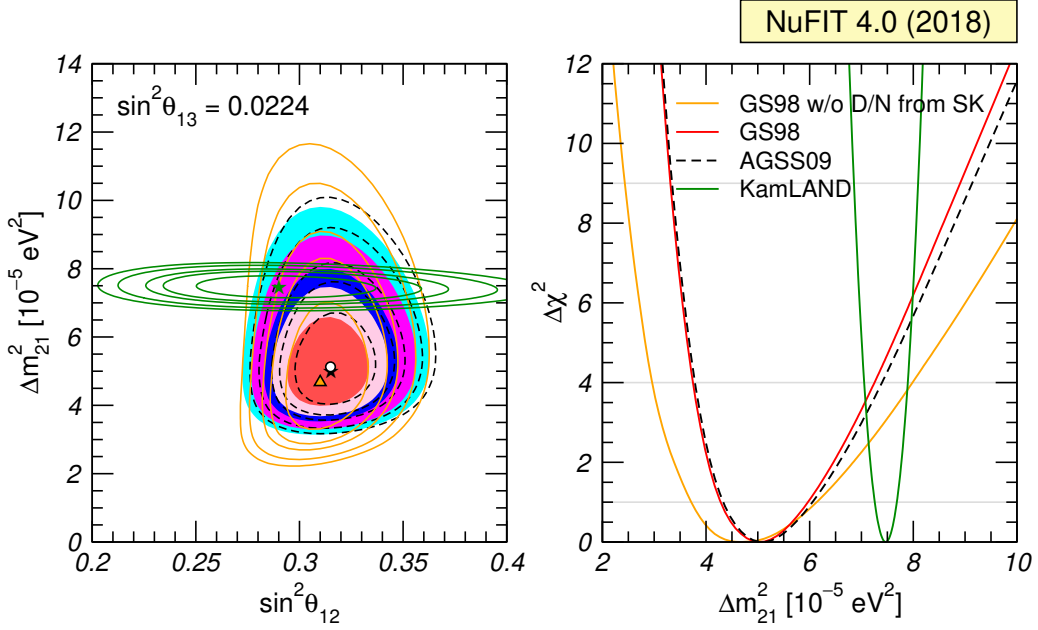


Figure 4. Left: Allowed parameter regions (at 1σ , 90%, 2σ , 99%, and 3σ CL for 2 dof) from the combined analysis of solar data for GS98 model (full regions with best fit marked by black star) and AGSS09 model (dashed void contours with best fit marked by a white dot), and for the analysis of KamLAND data (solid green contours with best fit marked by a green star) for fixed $\sin^2 \theta_{13} = 0.0224$ ($\theta_{13} = 8.6$). We also show as orange contours the results of a global analysis for the GS98 model but without including the day-night information from SK. Right: $\Delta\chi^2$ dependence on Δm_{21}^2 for the same four analyses after marginalizing over θ_{12} .

3.2 θ_{23} , δ_{CP} and mass ordering from LBL accelerator and MBL reactor experiments

The determination of the atmospheric parameters θ_{23} and $\Delta m_{3\ell}^2$ is illustrated in fig. 5. We observe significant synergy from combining the various experiments, since the combined region is clearly smaller than any individual one. Moreover, the striking agreement of LBL accelerator and MBL reactor data in the determination of $\Delta m_{3\ell}^2$ within comparable accuracy is a non-trivial cross check of the 3-flavour oscillation paradigm. Let us now discuss in more detail how the indication of non-maximal mixing and preference for the second octant for θ_{23} emerges.

3.2.1 Disappearance results and non-maximal θ_{23}

We focus first on LBL disappearance data. The ν_μ survival probability is given to good accuracy by [42, 43]

$$P_{\mu\mu} \approx 1 - \sin^2 2\theta_{\mu\mu} \sin^2 \frac{\Delta m_{\mu\mu}^2 L}{4E_\nu}, \quad (3.2)$$

where L is the baseline, E_ν is the neutrino energy, and

$$\sin^2 \theta_{\mu\mu} = \cos^2 \theta_{13} \sin^2 \theta_{23}, \quad (3.3)$$

$$\Delta m_{\mu\mu}^2 = \sin^2 \theta_{12} \Delta m_{31}^2 + \cos^2 \theta_{12} \Delta m_{32}^2 + \cos \delta_{\text{CP}} \sin \theta_{13} \sin 2\theta_{12} \tan \theta_{23} \Delta m_{21}^2. \quad (3.4)$$

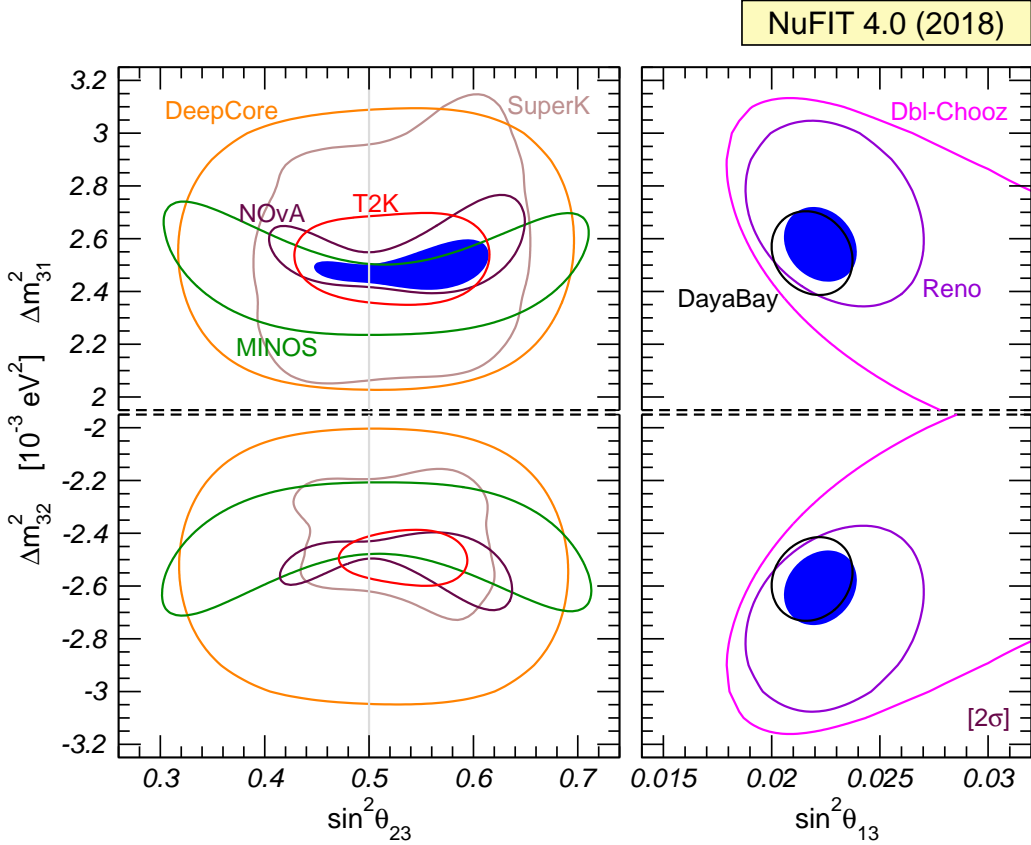


Figure 5. Determination of $\Delta m_{3\ell}^2$ at 2σ (2 dof), where $\ell = 1$ for NO (upper panels) and $\ell = 2$ for IO (lower panels). The left panels show regions in the $(\theta_{23}, \Delta m_{3\ell}^2)$ plane using both appearance and disappearance data from MINOS (green), T2K (red), NOvA (brown), as well as IceCube/DeepCore (orange), and SK-atm (from the table provided by the experiment, marron line) and the combination of them (blue coloured region). In the left panels the constraint on θ_{13} from the global fit (which is dominated by the reactor data) is imposed as a Gaussian bias. The right panels show regions in the $(\theta_{13}, \Delta m_{3\ell}^2)$ plane using only Daya Bay (black), Reno (violet) and Double Chooz (magenta) reactor data, and their combination (blue coloured region). In all panels Δm_{21}^2 , $\sin^2 \theta_{12}$ are fixed to the global best fit values. Contours are defined with respect to the global minimum of the two orderings.

Hence the survival probability is symmetric with respect to the octant of $\theta_{\mu\mu}$, which implies symmetry around $s_{23}^2 = 0.5/c_{13}^2 \approx 0.51$. This behaviour is visible in the left panels of fig. 6, which show the results of LBL accelerator disappearance data from MINOS, T2K, NOvA, separated into the neutrino and anti-neutrino data samples (for fixed value of θ_{13} at the best fit and NO). While most of the shown data samples prefer maximal mixing (especially T2K and NOvA neutrino data), maximal mixing is disfavoured by MINOS neutrino data ($\Delta\chi^2 \approx 2$) and NOvA anti-neutrino data ($\Delta\chi^2 \approx 6$). This behaviour can be traced back to the number of events in the corresponding data samples observed at the dip of the survival probability: for maximal mixing the survival probability is zero at the dip and no events should be observed. Qualitatively similar behaviour are found for IO.

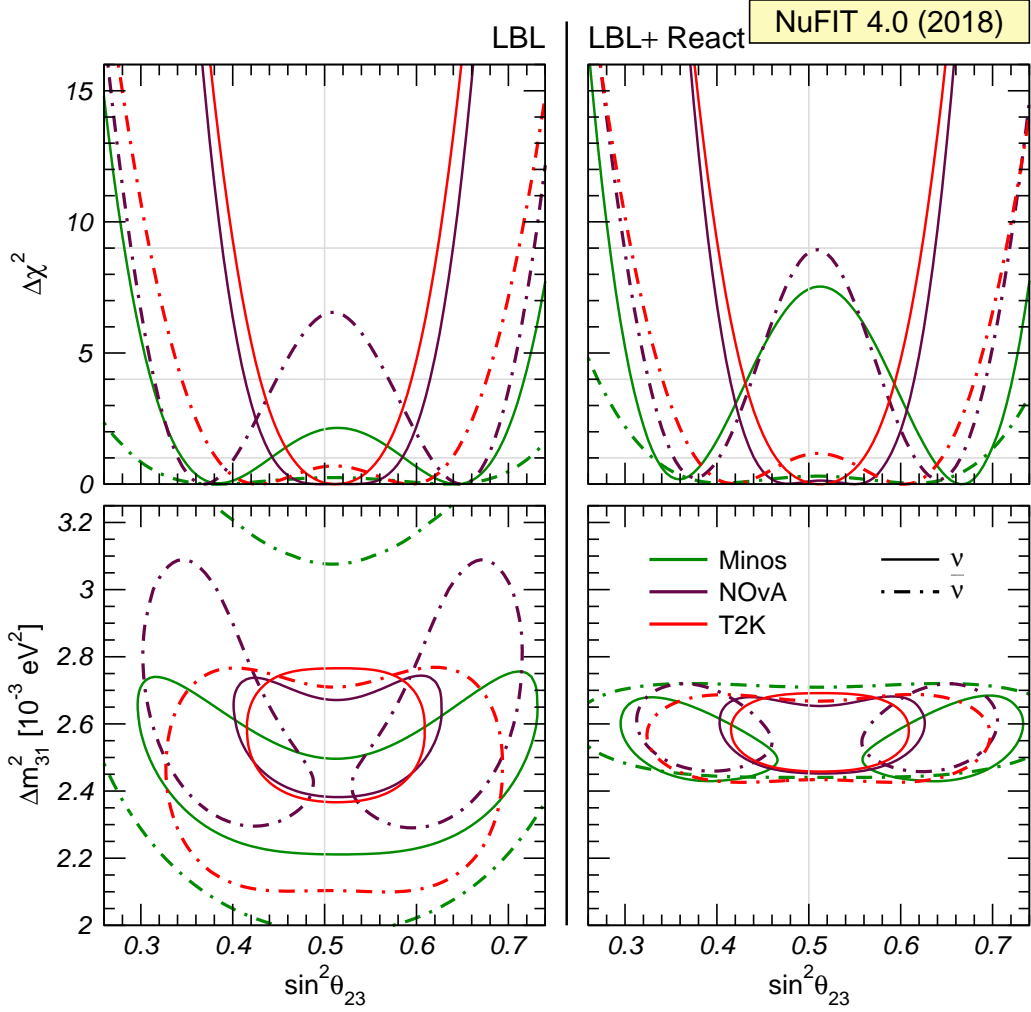


Figure 6. LBL accelerator ν_μ disappearance data only, from MINOS, T2K, and NOvA, separated into neutrino and anti-neutrino data. Left panels correspond to LBL accelerator data with constraint on θ_{13} from the global fit (which is dominated by the MBL reactor data) imposed as a Gaussian bias. In the right panels LBL data are consistently combined with MBL reactor data from Daya Bay, RENO, and Double Chooz. Upper panels show the $\Delta\chi^2$ as a function of $\sin^2\theta_{23}$, lower panels show confidence regions at 2σ (2 dof). All panels assume NO and Δm_{21}^2 , $\sin^2\theta_{12}$ are fixed to the global best fit values. Qualitatively similar behaviour is found in IO.

In the lower-left panel of fig. 6 we observe in addition a correlation between $\sin^2\theta_{23}$ and Δm_{31}^2 for the data which prefer non-maximal mixing: larger values of Δm_{31}^2 imply more deviation from maximal mixing. As visible in fig. 5, also MBL reactor data provide an accurate determination of $\Delta m_{3\ell}^2$, which, however, pushes slightly to larger values than LBL data. Because of the above mentioned correlation, this leads to an even stronger preference for non-maximal mixing, once LBL data are consistently combined with reactor data, as visible in the right panels of fig. 6: in combination with reactors, MINOS neutrino and NOvA anti-neutrino data disfavour maximal mixing with $\Delta\chi^2 \approx 7$ and 9, respectively.

3.2.2 Appearance results, second θ_{23} octant and δ_{CP}

The preference for the second octant of θ_{23} is driven by $\nu_\mu \rightarrow \nu_e$ appearance channel in LBL experiments (available both for neutrinos and anti-neutrinos). Following Ref. [32], the appearance probability can be approximated by

$$P_{\nu_\mu \rightarrow \nu_e} \approx 4s_{13}^2 s_{23}^2 (1 + 2oA) - C \sin \delta_{\text{CP}} (1 + oA), \quad (3.5)$$

$$P_{\bar{\nu}_\mu \rightarrow \bar{\nu}_e} \approx 4s_{13}^2 s_{23}^2 (1 - 2oA) + C \sin \delta_{\text{CP}} (1 - oA). \quad (3.6)$$

with

$$C \equiv \frac{\Delta m_{21}^2 L}{4E_\nu} \sin 2\theta_{12} \sin 2\theta_{13} \sin 2\theta_{23}, \quad o \equiv \text{sgn}(\Delta m_{3\ell}^2), \quad A \equiv \left| \frac{2E_\nu V}{\Delta m_{3\ell}^2} \right|, \quad (3.7)$$

where V is the effective matter potential. In the above equations we have expanded in the small parameters s_{13} , $\Delta m_{21}^2 L/E_\nu$, and A , and used that for T2K and NOvA $|\Delta m_{3\ell}^2| L/4E_\nu \approx \pi/2$.² Using the respective mean neutrino energies we find $A \approx 0.05$ for T2K and an *empirical* value of $A = 0.1$ (for which this approximation works better) at NOvA. Correspondingly the number of observed appearance events in T2K and NOvA is approximately proportional to the oscillation probability:

$$N_{\nu_e} \approx \mathcal{N}_\nu [2s_{23}^2 (1 + 2oA) - C' \sin \delta_{\text{CP}} (1 + oA)], \quad (3.8)$$

$$N_{\bar{\nu}_e} \approx \mathcal{N}_{\bar{\nu}} [2s_{23}^2 (1 - 2oA) + C' \sin \delta_{\text{CP}} (1 - oA)]. \quad (3.9)$$

Taking all the well-determined parameters θ_{13} , θ_{12} , Δm_{21}^2 , $|\Delta m_{3\ell}^2|$ at their global best fit points, we obtain numerically $C' \approx 0.28$. The normalization constants $\mathcal{N}_{\nu, \bar{\nu}}$ calculated from our re-analysis of T2K and NOvA are given for the various appearance samples in table 2. Those values can be compared with the background subtracted observed number of events, which we also report in the table. Within this approximation, there are only the two parameters s_{23}^2 and $\sin \delta_{\text{CP}}$, plus the discrete parameter $o = \pm 1$ encoding the mass ordering, to fit the appearance event numbers shown in table 2, with $\sin^2 \theta_{23}$ being constrained in addition from disappearance data. Note that C' depends only on $\sin 2\theta_{23}$, which varies by less than 2% for $0.42 < s_{23}^2 < 0.64$, and can be taken as constant for our purposes. The general trends from eqs. (3.8) and (3.9) are the following:

- Both neutrino and anti-neutrino events are enhanced by increasing s_{23}^2 .
- Values of $\sin \delta_{\text{CP}} \simeq +1$ (-1) suppress (increase) neutrino events, and have the opposite effect for anti-neutrino events.
- For NO (IO) neutrino events are enhanced (suppressed) due to the matter effect, whereas anti-neutrino events are suppressed (enhanced).
- For NO (IO) the matter effect increases (decreases) the impact of δ_{CP} for neutrinos, while the opposite happens for anti-neutrinos.

²Expanding in the matter potential parameter A is a very good approximation for T2K, but not so good for NOvA. However, the qualitative behaviour is still captured by the above expressions also for NOvA, which suffices for our discussion here.

	T2K CCQE (ν)	T2K CC1 π (ν)	T2K CCQE ($\bar{\nu}$)	NOvA (ν)	NOvA ($\bar{\nu}$)
\mathcal{N}	40	3.8	11	34	11
N_{obs}	75	15	9	58	18
$N_{\text{obs}} - N_{\text{bck}}$	61.4	13.6	6.1	43.6	13.8

Table 2. Normalization coefficients \mathcal{N}_ν and $\mathcal{N}_{\bar{\nu}}$ for eqs. (3.8) and (3.9) for approximations used to qualitatively describe the various appearance event samples used in our analysis for T2K and NOvA. We also give the observed number of events, as well as the corresponding background subtracted event numbers, as reported in Refs. [44, 45]

The last two items are more important for NOvA than for T2K, due to larger matter effects in NOvA because of the longer baseline.

In fig. 7, the determination of s_{23}^2 from LBL data (including appearance) combined with reactor data is shown. In the upper panels only θ_{13} is constrained by reactor data, whereas in the lower panels LBL and reactor data are combined consistently, including also $\Delta m_{3\ell}^2$ information. For the reasons explained above, lower panels show larger significance of non-maximality, but now the symmetry between the octants is broken by appearance data. Fig. 8 shows the $\Delta\chi^2$ dependence on δ_{CP} for various data samples.

Let us consider first the T2K samples. We see from table 2 that in both neutrino samples (especially CC1 π) the observed number of events after background subtraction is large compared to \mathcal{N}_ν , while the anti-neutrino number is low. Hence, we need to maximize the expression in eq. (3.8) and minimize eq. (3.9). Since neutrino data dominates over anti-neutrinos, a slight preference for $s_{23}^2 > 0.5$ appears (constrained by disappearance data), while at the same time $\sin \delta_{\text{CP}} \approx -1$ serves to maximize (minimize) neutrino (anti-neutrino) appearance, as visible in fig. 8.

For NOvA neutrino data, the coefficient \mathcal{N}_ν in eq. (3.8) is also somewhat low compared to the observed number of events minus background. For NO, the matter effect enhances neutrino events, and therefore, s_{23}^2 (around maximal mixing favoured in disappearance) and δ_{CP} can be adjusted, such that the event numbers can always be fitted, so $\Delta\chi^2(\delta_{\text{CP}})$ from NOvA neutrino data alone is < 1 for NO, cf. fig. 8. For IO, however, the matter effect suppresses neutrino events, and therefore, preference for the second octant and $\sin \delta_{\text{CP}} \approx -1$ appears to maximize the term in the square-bracket in eq. (3.8). For NOvA anti-neutrino data, table 2 shows that the observed event number is of the order of $\mathcal{N}_{\bar{\nu}}$ (only slightly higher). Consequently we observe for NO only a very mild preference for $\sin \delta_{\text{CP}} \approx 1$ just to enhance slightly the rate of anti-neutrinos. For IO, the matter effect enhances anti-neutrinos, and therefore, choosing the combinations (first θ_{23} octant/ $\sin \delta_{\text{CP}} \approx 1$) or (second θ_{23} octant/ $\sin \delta_{\text{CP}} \approx -1$) can fit the events, which leads to negligible $\Delta\chi^2(\delta_{\text{CP}})$ dependence for IO NOvA anti-neutrinos, cf. fig. 8. The combination of those effects for NO, leads to a disfavouring of $\sin \delta_{\text{CP}} \approx -1$ with $\Delta\chi^2 \approx 3.5$ from NOvA, somewhat in contradiction of the T2K preferred region: with the non-maximality of θ_{23} from anti-neutrinos plus the matter enhancement for neutrinos, $\sin \delta_{\text{CP}} \approx -1$ would predict too many neutrino events, and is therefore disfavoured.

The conclusion of those considerations lead to the preference of the second octant for θ_{23} in the global analysis, as well as pushing the confidence interval for δ_{CP} towards 180° ,

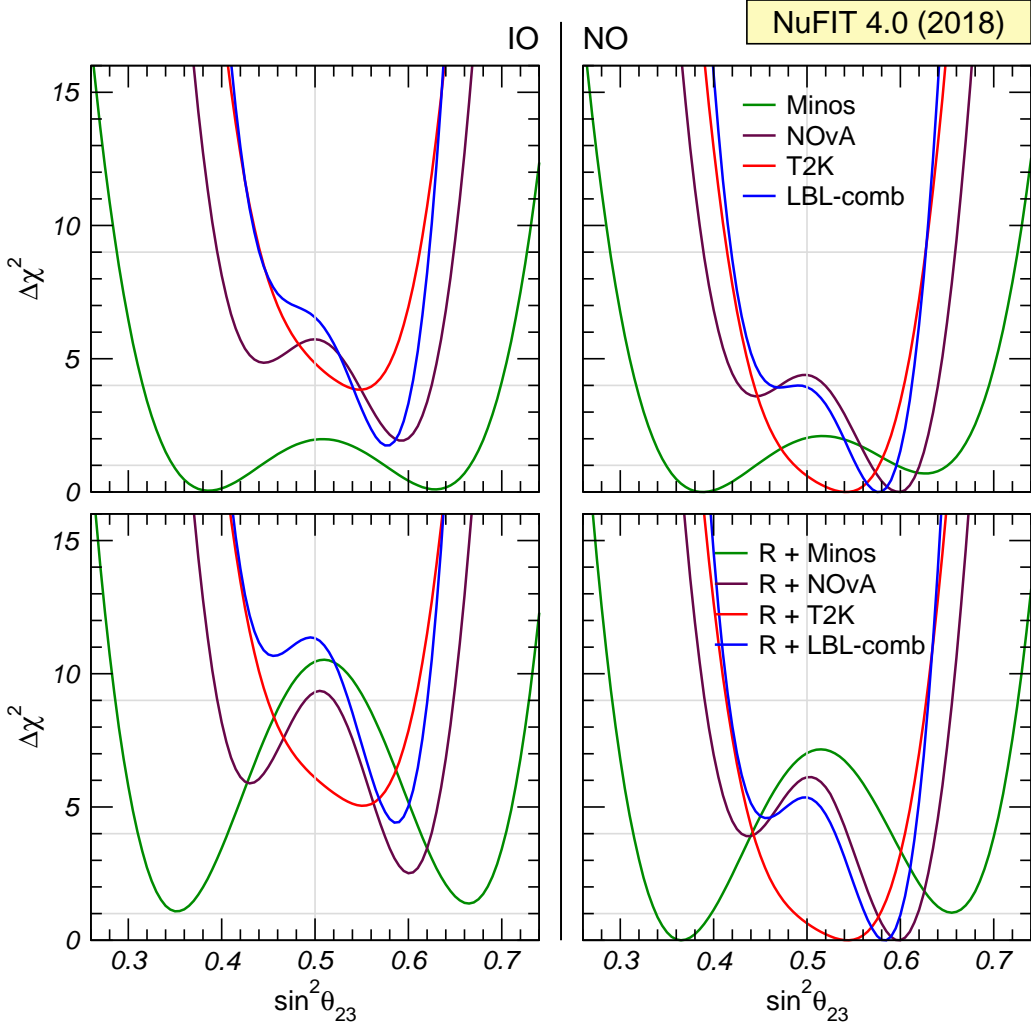


Figure 7. θ_{23} determination from LBL, reactor and their combination. Left (right) panels are for IO (NO). The upper panels show the 1-dim $\Delta\chi^2$ from LBL experiments after constraining *only* θ_{13} from reactor experiments. For each experiment $\Delta\chi^2$ is defined with respect to the global minimum of the two orderings. The lower panels show the corresponding determination when the full information of LBL accelerator and reactor experiments is used in the combination (including the information on $\Delta m_{3\ell}^2$ from reactors). In all panels Δm_{21}^2 , $\sin^2\theta_{12}$ are fixed to the global best fit values.

which implies that CP conservation is allowed by the combined data with $\Delta\chi^2 \approx 1.5$.

3.2.3 Preference for normal ordering

An important result of the present global fit is the growing significance of the preference for the normal mass ordering. This indication emerges by a subtle interplay of various subsets of the global data. Sensitivity to the mass ordering is provided by the matter effect [38, 39, 46] in oscillations with $\Delta m_{3\ell}^2$, observable in LBL accelerator and atmospheric neutrino experiments, as well as the comparison oscillations in the ν_e and ν_μ disappearance channels [43, 47, 48].

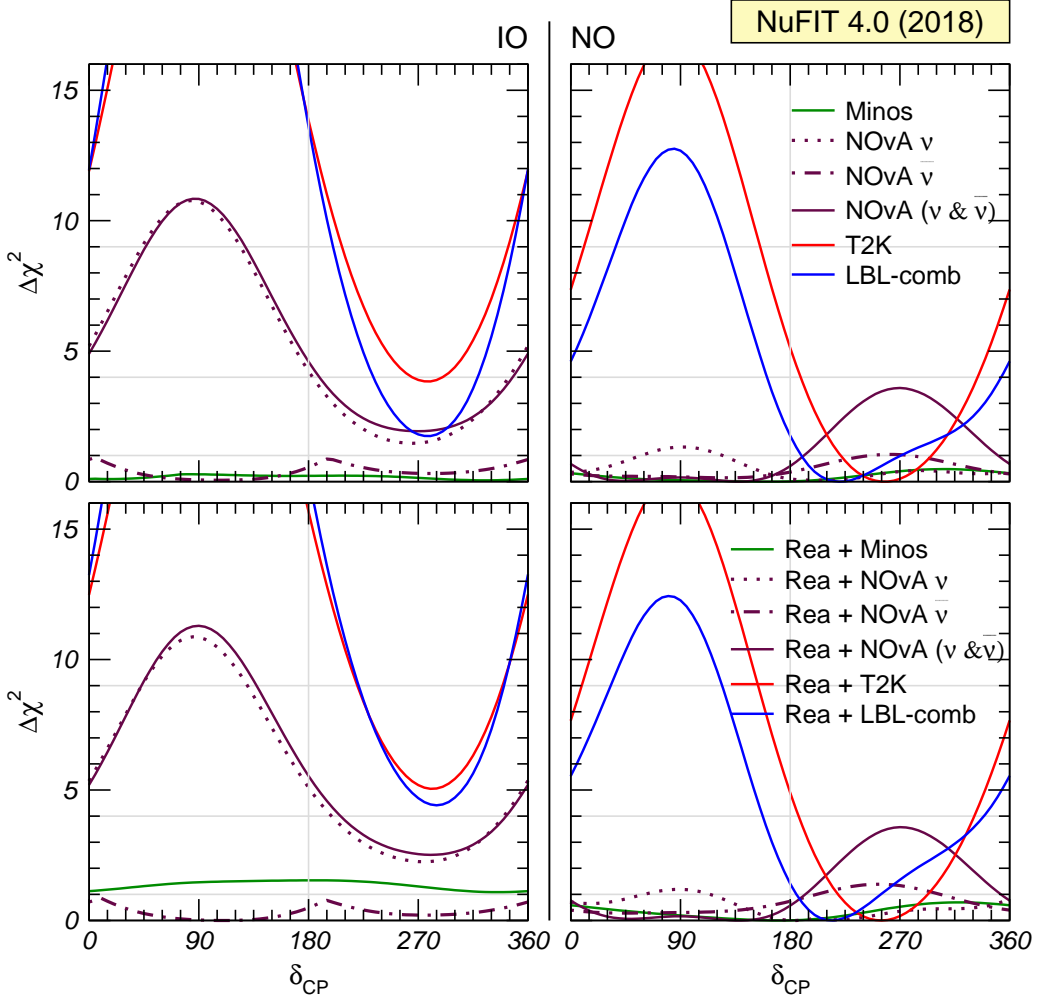


Figure 8. δ_{CP} determination from LBL, reactor and their combination. Left (right) panels are for IO (NO). The upper panels show the 1-dim $\Delta\chi^2$ from LBL experiments after constraining *only* θ_{13} from reactor experiments. For each experiment $\Delta\chi^2$ is defined with respect to the global minimum of the two orderings. The lower panels show the corresponding determination when the full information of LBL accelerator and reactor experiments on both mixing angles and $\Delta m_{3\ell}^2$ is used in the combination. In all panels Δm_{21}^2 , $\sin^2 \theta_{12}$ are fixed to the global best fit values.

Let us first discuss the indication coming from LBL accelerator experiments. We find that T2K + the θ_{13} constraint from reactors disfavors IO by $\Delta\chi^2 \approx 4$, see upper panels of figs. 7, 8 and 9. This can be understood from the numbers in table 2 and eqs. (3.8) and (3.9), where the matter effect for NO helps to increase (decrease) events for neutrinos (anti-neutrinos). NOvA data + the θ_{13} constraint also disfavors IO by about 2 units in χ^2 , driven by neutrino data, while anti-neutrinos are insensitive to the ordering, cf. fig. 8. Interestingly, by combining T2K, NOvA, and MINOS, *decreases* the $\Delta\chi^2$ of IO to about 2. An explanation for this effect is the slight tension between NOvA and T2K in the determination of δ_{CP} for NO visible in fig. 8. This leads to a worse fit of NO compared to IO, where both experiments prefer the same region for δ_{CP} .

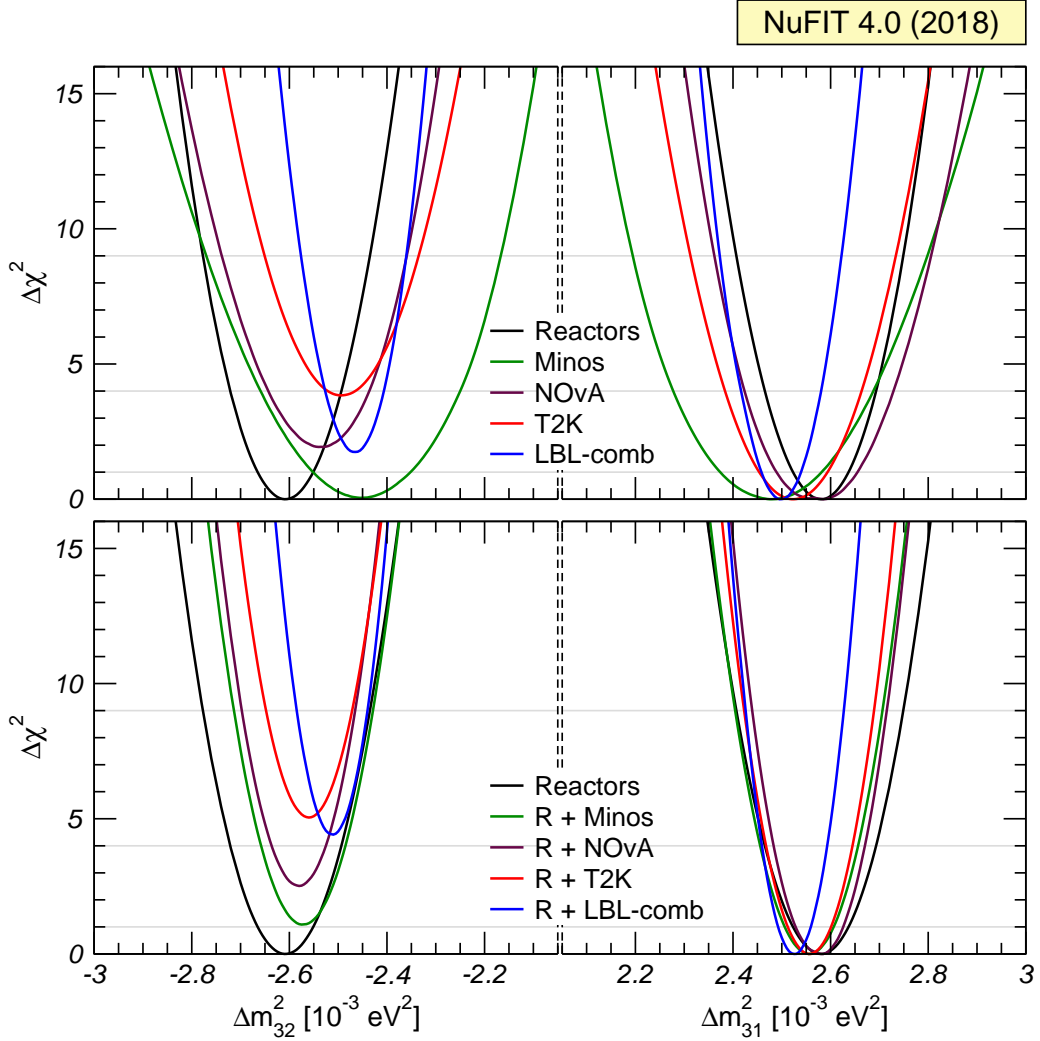


Figure 9. $\Delta m_{3\ell}^2$ determination from LBL, reactor and their combination. Left (right) panels are for IO (NO). The upper panels show the 1-dim $\Delta\chi^2$ from LBL experiments after constraining *only* θ_{13} from reactor experiments. For each experiment $\Delta\chi^2$ is defined with respect to the global minimum of the two orderings. The lower panels show the corresponding determination when the full information of LBL accelerator and reactor experiments is used in the combination (including the information on $\Delta m_{3\ell}^2$ from reactors). In all panels Δm_{21}^2 , $\sin^2\theta_{12}$ are fixed to the global best fit values.

An interesting additional effect sensitive to the mass ordering has been pointed out in Refs. [43, 47]: the ν_μ disappearance probability is symmetric with respect to the sign of $\Delta m_{\mu\mu}^2$ given in eq. (3.4), while ν_e disappearance is symmetric with respect to a slightly different effective mass-squared difference:

$$\Delta m_{ee}^2 = \cos^2\theta_{12}\Delta m_{31}^2 + \sin^2\theta_{12}\Delta m_{32}^2. \quad (3.10)$$

Hence, from a precise determination of the oscillation frequencies in ν_μ and ν_e disappear-

ance experiments, information on the sign of $\Delta m_{3\ell}^2$ can be obtained.³ Indeed, we observe in fig. 9 that this effect already contributes notably to the mass ordering discrimination in present data: the upper panels show the determination of $\Delta m_{3\ell}^2$ from the individual LBL accelerator experiments (ν_μ disappearance) compared to the one from MBL reactors (ν_e disappearance). We have verified that those curves are indeed symmetric with respect to the sign of $\Delta m_{\mu\mu}^2$ and Δm_{ee}^2 , respectively, within excellent accuracy. When displaying them for common parameters ($\Delta m_{3\ell}^2$ in fig. 9), we observe that the agreement is better for NO than for IO. The difference between the upper and lower panels in the $\Delta\chi^2$ for IO is largely due to this $\Delta m_{3\ell}^2$ effect. We see that the $\Delta\chi^2$ for the LBL combination is pushed from 2 to about 4.5, when combined consistently with reactor data taking into account the $\Delta m_{3\ell}^2$ dependence.

In summary, we obtain from LBL+reactor data a preference for NO at about 2σ . As mentioned in section 2.2, this gets further enhanced by atmospheric neutrino data, with the main contribution from Super-Kamiokande, leading to the exclusion of IO at about 3σ , see fig. 1. In the following subsection we discuss in more detail various aspects of the atmospheric neutrino analyses from IceCube and Super-Kamiokande.

3.3 Treatment of atmospheric results from Super-Kamiokande and Deep-Core

In what respects the atmospheric neutrino data, in our default analysis – full lines in figs. 1 and 3 (one-dimensional $\Delta\chi^2$ curves) and coloured regions in fig. 2 (two-dimensional projections of confidence regions) – we include the results of the Deep-Core 3-years data of Ref. [27, 28] (which we refer here as DC16) for which the collaboration has provided enough information on their effective areas to allow for our own reanalysis. Its impact in the parameter determination obtained from the combination of solar, reactor and LBL data is very marginal, see fig. 10, which displays as example its contribution to the determination of $\Delta m_{3\ell}^2$ and the ordering where it adds about 0.3 units to χ_{\min}^2 of IO because of the slightly better matching between the $\Delta m_{3\ell}^2$ from reactor+LBL experiments with that of DC in NO.⁴

In this respect it is interesting to notice that the ICECUBE collaboration has recently published the results of a dedicated analysis of another set of three-years data [31, 49] leading to a better determination of $\Delta m_{3\ell}^2$ (which we refer to as DC17). Unfortunately we cannot reproduce this analysis because the corresponding effective areas have not been made public. The experiment has only made available the bi-dimensional χ^2 map (as a function of $\Delta m_{3\ell}^2$ and $\sin^2\theta_{23}$ for a fixed value of $\sin^2\theta_{13} = 0.0217$ and $\delta_{\text{CP}} = 0$) corresponding to that analysis. Strictly this cannot be added in the global analysis without making some assumption about their possible θ_{13} and δ_{CP} dependence. Still, to illustrate the possible impact of using these results we show also in fig. 10 the corresponding contribution to the determination of $\Delta m_{3\ell}^2$ and the ordering obtained by naively adding their χ^2 map to our results of the global reactor+LBL experiments (neglecting any possible depen-

³A similar effect has been exploited in Ref. [48], based on the comparison of the $\Delta m_{3\ell}^2$ determination in future reactor and atmospheric neutrino experiments.

⁴All curves in fig. 10 contain the bias on Δm_{21}^2 and θ_{12} from solar and KamLAND, so the full lines denoted as R+LBL+DC16 coincide with the corresponding full lines in the corresponding panel in fig. 1.

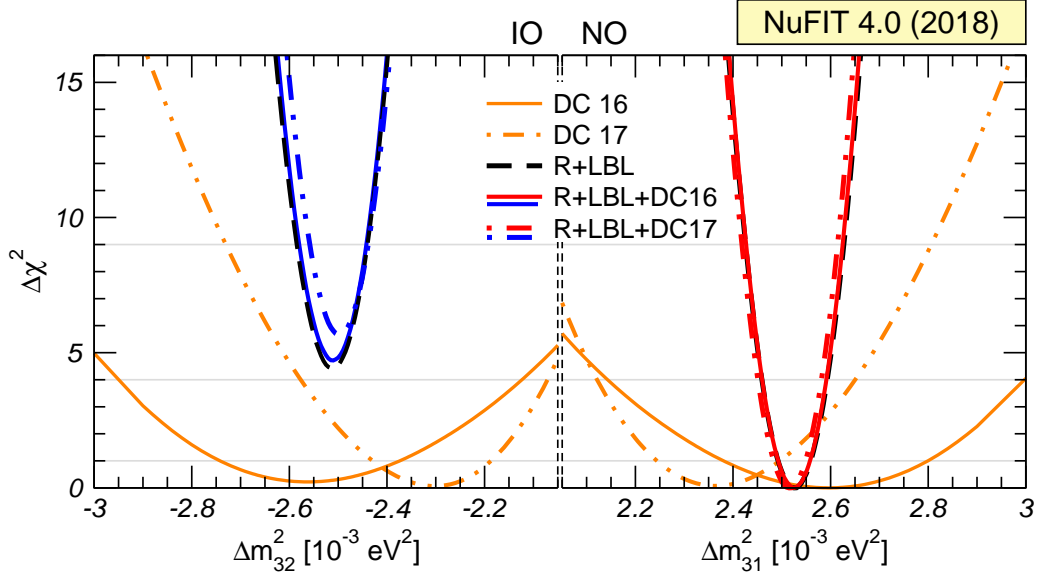


Figure 10. $\Delta\chi^2$ as a function of $\Delta m_{3\ell}^2$ for our reanalysis of Deep-Core 3-years data of Ref. [27, 28] (labeled DC16, solid orange line) and its combination with the global analysis of reactor and LBL experiments (full blue and red lines). The corresponding dash-dotted line correspond to use the χ^2 table provided by the experiment for the analysis of their three years data in Ref. [31, 49] (labeled DC17). See text for details.

dence on the fixed parameters). As seen in the figure, using the DC17 results in the global combination disfavors IO by ~ 1.2 additional units of χ^2 . One must notice, however, that the ICECUBE collaboration has recently performed a reanalysis of the same data sample which leads to similar precision but a somewhat shifted range for $\Delta m_{3\ell}^2$ [50].

In what respects to the results of Super-Kamiokande, in the last five years the collaboration has developed a more sophisticated analysis method for their atmospheric neutrino data with the aim of constructing $\nu_e + \bar{\nu}_e$ enriched samples which are then further classified into ν_e -like and $\bar{\nu}_e$ -like subsamples, thus increasing the sensitivity to subleading parameters such as the mass ordering and δ_{CP} . The official results obtained with this method were published in Ref. [29] and show – once θ_{13} is constrained to be within the range determined by reactor experiments – a preference for NO with a $\Delta\chi^2(\text{IO}) = 4.3$, variation of $\chi^2(\delta_{\text{CP}})$ with the CP phase at the level of $\sim 90\%$ CL (with favouring $\delta_{\text{CP}} \sim 270^\circ$), and a slight favouring of the second octant of θ_{23} (see fig.14 in Ref. [29]).

Unfortunately with the information at hand we are not able to reproduce the elements driving the main dependence on these subdominant oscillation effects in our own reanalysis of the data samples which can be simulated outside of the collaboration. However, Super-Kamiokande has also published the results of their analysis in the form of a tabulated χ^2 map [30] as a function of the four relevant parameters $\Delta m_{3\ell}^2, \theta_{23}, \theta_{13}$, and δ_{CP} which we can add to our global analysis χ^2 in the multidimensional parameter space in a fully consistent form and then perform the corresponding parameter marginalization to obtain the combined one-dimensional or two dimensional parameter ranges. The results of such

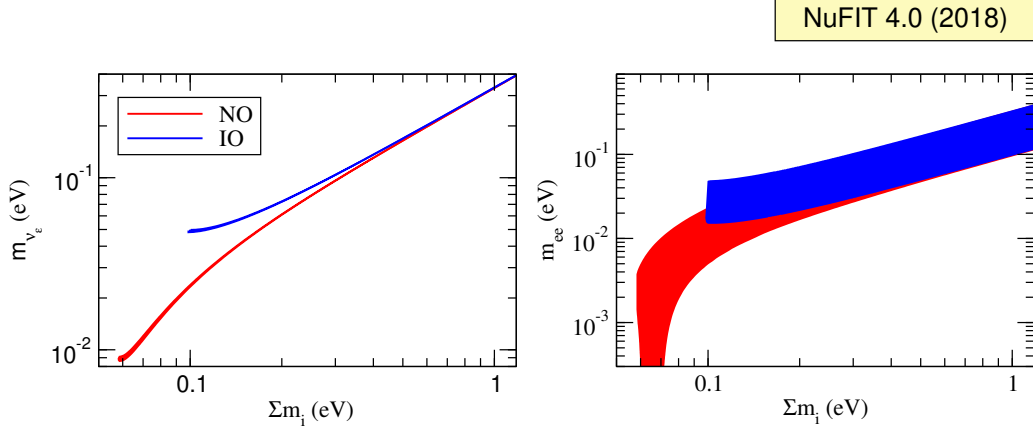


Figure 11. 95% allowed regions (for 2 dof) in the planes $(m_{\nu_e}, \sum m_\nu)$ and $(m_{ee}, \sum m_\nu)$ obtain from projecting the results of the global analysis of oscillation data. The regions are defined with respect to the minimum for each ordering.

combination are shown as dashed curves in in figs. 1 and 3 (one-dimensional $\Delta\chi^2$ curves) and void regions in fig. 2 (two-dimensional projections of confidence regions). As can be seen from fig. 1, adding the SK-atm χ^2 information results into:

- Increase of the χ_{\min}^2 for IO by 4.6 units (from 4.7 to 9.3).
- Enhancement of the parameter dependence of $\chi^2(\delta_{\text{CP}})$ further disfavouring δ_{CP} values around 90° (for example it increases $\chi^2(\delta_{\text{CP}} = 70^\circ)$ in NO by ~ 3 units from ~ 13 to ~ 16)
- Enhancement of the parameter dependence of $\chi^2(s_{23}^2)$ further disfavouring the first octant (for example it increases $\chi^2(s_{23}^2 = 0.45\text{--}0.5)$ in NO by ~ 2 units.

In other words, as the SK-atm tendencies for these subdominant effects are very well aligned with those from the combination of LBL experiments (currently dominated by T2K), their impact in the determination of δ_{CP} and θ_{23} in the global analysis is almost equivalent to just adding for each of those parameters their marginalized χ^2 (with fixed θ_{13} at the reactor value) to that from the global analysis without SK-atm.

4 Projections on neutrino mass scale observables

Oscillation experiments provide information on the mass-squared splittings Δm_{ij}^2 and on the leptonic mixing angles U_{ij} , but they are insensitive to the absolute mass scale for the neutrinos. Of course, the results of an oscillation experiment do provide a lower bound on the heavier mass in Δm_{ij}^2 , $|m_i| \geq \sqrt{\Delta m_{ij}^2}$ for $\Delta m_{ij}^2 > 0$, but there is no upper bound on this mass. In particular, the corresponding neutrinos could be approximately degenerate at a mass scale that is much higher than $\sqrt{\Delta m_{ij}^2}$. Moreover, there is neither an upper nor a lower bound on the lighter mass m_j .

Information on the neutrino masses, rather than mass differences, can be extracted from kinematic studies of reactions in which a neutrino or an anti-neutrino is involved. In the presence of mixing the most relevant constraint comes from the study of the end point ($E \sim E_0$) of the electron spectrum in Tritium beta decay ${}^3\text{H} \rightarrow {}^3\text{He} + e^- + \bar{\nu}_e$. This spectrum can be effectively described by a single parameter, m_{ν_e} , if for all neutrino states $E_0 - E \gg m_i$:

$$m_{\nu_e}^2 = \frac{\sum_i m_i^2 |U_{ei}|^2}{\sum_i |U_{ei}|^2} = \sum_i m_i^2 |U_{ei}|^2 = c_{13}^2 c_{12}^2 m_1^2 + c_{13}^2 s_{12}^2 m_2^2 + s_{13}^2 m_3^2$$

$$= \begin{cases} \text{NO:} & m_0^2 + \Delta m_{21}^2 c_{13}^2 s_{12}^2 + \Delta m_{3\ell}^2 s_{13}^2, \\ \text{IO:} & m_0^2 - \Delta m_{21}^2 c_{13}^2 c_{12}^2 - \Delta m_{3\ell}^2 c_{13}^2 \end{cases} \quad (4.1)$$

where the second equality holds if unitarity is assumed and $m_0 = m_1$ (m_3) in NO (IO) denotes the lightest neutrino mass. At present we only have an upper bound, $m_{\nu_e} \leq 2.2$ eV at 95% CL [51], which is expected to be superseded soon by KATRIN [52] with about one order of magnitude improvement in sensitivity.

Direct information on neutrino masses can also be obtained from neutrinoless double beta decay $(A, Z) \rightarrow (A, Z + 2) + e^- + e^-$. This process violates lepton number by two units, hence in order to induce the $0\nu\beta\beta$ decay, neutrinos must be Majorana particles. In particular, for the case in which the only effective lepton number violation at low energies is induced by the Majorana mass term for the neutrinos, the rate of $0\nu\beta\beta$ decay is proportional to the *effective Majorana mass of ν_e* :

$$m_{ee} = \left| \sum_i m_i U_{ei}^2 \right| = \left| m_1 c_{13}^2 c_{12}^2 e^{i2\alpha_1} + m_2 c_{13}^2 s_{12}^2 e^{i2\alpha_2} + m_3 s_{13}^2 e^{-i2\delta_{\text{CP}}} \right|$$

$$= \begin{cases} \text{NO:} & m_0 \left| c_{13}^2 c_{12}^2 e^{i2(\alpha_1 - \delta_{\text{CP}})} + \sqrt{1 + \frac{\Delta m_{21}^2}{m_0^2}} c_{13}^2 s_{12}^2 e^{i2(\alpha_2 - \delta_{\text{CP}})} + \sqrt{1 + \frac{\Delta m_{3\ell}^2}{m_0^2}} s_{13}^2 \right| \\ \text{IO:} & m_0 \left| \sqrt{1 - \frac{\Delta m_{3\ell}^2 + \Delta m_{21}^2}{m_0^2}} c_{13}^2 c_{12}^2 e^{i2(\alpha_1 - \delta_{\text{CP}})} + \sqrt{1 - \frac{\Delta m_{3\ell}^2}{m_0^2}} c_{13}^2 s_{12}^2 e^{i2(\alpha_2 - \delta_{\text{CP}})} + s_{13}^2 \right| \end{cases} \quad (4.2)$$

which, unlike Eq. (4.1), depends also on the CP violating phases. Recent searches have established the lifetime of this decay to be longer than $\sim 10^{26}$ yr [53, 54], corresponding to a limit on the neutrino mass of $m_{ee} \lesssim 0.06 - 0.200$ eV at 90% CL. A series of new experiments is planned with sensitivity of up to $m_{ee} \sim 0.01$ eV [55].

Neutrino masses have also interesting cosmological effects. In general, cosmological data mostly give information on the sum of the neutrino masses, $\sum_i m_i$, while they have very little to say on their mixing structure and on the ordering of the mass states.

Correlated information on these three probes of the neutrino mass scale can be obtained by mapping the results from the global analysis of oscillations presented previously. We show in fig. 11 the present status of this exercise. The relatively large width of the regions in the right panel are due to the unknown Majorana phases. Thus from a positive determination of two of these probes, in principle information can be obtained on the value of the Majorana phases and/or the mass ordering [56, 57].

5 Conclusions

We have presented the results of the updated (as of fall 2018) analysis of relevant neutrino data in the framework of mixing among three massive neutrinos. We have shown our results for two analyses. The first contains our own statistical combination of all the experimental data for which we are able to reproduce the results of the partial analysis performed by the different experiments, and therefore does not include the information of the Super-Kamiokande atmospheric neutrino data. In the second analysis we combine the likelihood of the first one with the four-dimensional χ^2 map provided by Super-Kamiokande for the analysis of their atmospheric data. Quantitatively the present determination of the two mass differences, three mixing angles and the relevant CP violating phase for the two analysis is listed in table 1, and the corresponding leptonic mixing matrix is given in Eq. (2.2). In both analysis the maximum allowed CP violation in the leptonic sector parametrized by the Jarlskog determinant is $J_{\text{CP}}^{\text{max}} = 0.0333 \pm 0.0006 (\pm 0.0019)$ at 1σ (3σ).

We have performed a detail study of the role of the different data samples and their correct combination in the determination of the less known parameters, θ_{23} , δ_{CP} and the ordering in section 3. We can summarize the main conclusions in this section as follows:

- The long standing tension between the best Δm_{21}^2 determined in the solar neutrino analysis and that from KamLAND persists. The inclusion of latest spectral data from SK4 and the use of Daya Bay near detector data for reactor flux normalization in KamLAND has made this tension slightly stronger, but it is still a $\sim 2\sigma$ effect.
- We obtain preference for the second octant of θ_{23} in the global analysis with a best fit at $\sin^2 \theta_{23} = 0.58$. There are two effects contributing to this results:
 - While most data samples in ν_μ and $\bar{\nu}_\mu$ disappearance at LBL prefer close to maximal mixing (especially T2K and NOvA neutrino data), maximal mixing is disfavoured by MINOS neutrino data ($\Delta\chi^2 \approx 2$) and NOvA anti-neutrino data ($\Delta\chi^2 \approx 6$). This disfavouring increases when fully combining with the reactor neutrino determination of $\Delta m_{3\ell}^2$ to $\Delta\chi^2 \approx 7$ and 9, respectively.
 - The appearance results both in T2K and NOvA (SK-atm adds in the same direction) favour the second octant. The final value of the best fit θ_{23} results of this effect in combination with the substantial non-maximality favoured by NOvA anti-neutrino and MINOS neutrino disappearance data.
- The determination of δ_{CP} is mostly driven by T2K neutrino and anti-neutrino appearance results which favour $\delta_{\text{CP}} \sim 3\pi/2$ and disfavours $\delta_{\text{CP}} \sim \pi/2$ for both NO and IO. NOvA neutrino appearance data align with this behaviour, and are more statistically significant in IO. On the contrary NOvA anti-neutrino appearance data are better (worse) described with $\delta_{\text{CP}} \sim \pi/2$ ($\delta_{\text{CP}} \sim 3\pi/2$) in NO. This slight tension results into a shift of the best fit to $\delta_{\text{CP}} = 215^\circ$ in NO. So the allowed range is pushed towards the CP conserving value of 180° , which now is only disfavoured with $\Delta\chi^2 \lesssim 2$.

- Regarding the mass ordering:
 - Both T2K and NOvA prefer NO individually: T2K (NOvA) + the θ_{13} constraint from reactors disfavors IO by $\Delta\chi^2 \approx 4$ (2), but combining T2K, NOvA (and MINOS) *decreases* the $\Delta\chi^2$ of IO to about 2. This is a consequence of the slight tension between NOvA and T2K in the determination of δ_{CP} for NO.
 - Additional sensitivity to the ordering is found by the precise determination of the oscillation frequency in ν_μ and ν_e disappearance data at LBL and reactors, respectively. This effect increases $\Delta\chi^2$ of IO from 2 to about 4.5.
 - Inclusion of the atmospheric neutrino results (mainly from SK) further increases $\Delta\chi^2$ of IO to the 3σ level.

Future updates of this analysis will be provided at the NuFIT website quoted in Ref. [12].

Acknowledgments

This work is supported by USA-NSF grant PHY-1620628, by EU Networks FP10 ITN ELUSIVES (H2020-MSCA-ITN-2015-674896) and INVISIBLES-PLUS (H2020-MSCA-RISE-2015-690575), by MINECO grant FPA2016-76005-C2-1-P and MINECO/FEDER-UE grants FPA2015-65929-P and FPA2016-78645-P, by Maria de Maetzu program grant MDM-2014-0367 of ICCUB, and by the ‘‘Severo Ochoa’’ program grant SEV-2016-0597 of IFT. I.E. acknowledges support from the FPU program fellowship FPU15/03697.

A List of data used in the analysis

Solar experiments

- *External information:* Standard Solar Model [37].
- Chlorine total rate [58], 1 data point.
- Gallex & GNO total rates [59], 2 data points.
- SAGE total rate [60], 1 data point.
- SK1 full energy and zenith spectrum [61], 44 data points.
- SK2 full energy and day/night spectrum [62], 33 data points.
- SK3 full energy and day/night spectrum [63], 42 data points.
- SK4 2055-day day-night asymmetry [41] and 2860-day energy spectrum [40], 24 data points.
- SNO combined analysis [64], 7 data points.
- Borexino Phase-I 741-day low-energy data [65], 33 data points.
- Borexino Phase-I 246-day high-energy data [66], 6 data points.
- Borexino Phase-II 408-day low-energy data [67], 42 data points.

Atmospheric experiments

- *External information:* Atmospheric neutrino fluxes [68].
- IceCube/DeepCore 3-year data [27, 28], 64 data points.
- SK1-4 328 kiloton years [29], χ^2 map [30] added to our global analysis.

Reactor experiments

- KamLAND separate DS1, DS2, DS3 spectra [69] with Daya Bay reactor ν fluxes [25], 69 data points.
- Double Chooz FD-I/ND and FD-II/ND spectral ratios, with 455-day (FD-I), 363-day (FD-II) and 258-day (ND) exposures [70], 56 data points.
- Daya Bay 1958-day EH2/EH1 and EH3/EH1 spectral ratios [21], 52 data points.
- Reno 2200-day FD/ND spectral ratios [22], 26 data points.

Accelerator experiments

- MINOS 10.71×10^{20} pot ν_μ -disappearance data [15], 39 data points.
- MINOS 3.36×10^{20} pot $\bar{\nu}_\mu$ -disappearance data [15], 14 data points.
- MINOS 10.6×10^{20} pot ν_e -appearance data [16], 5 data points.
- MINOS 3.3×10^{20} pot $\bar{\nu}_e$ -appearance data [16], 5 data points.
- T2K 14.93×10^{20} pot ν_μ -disappearance data [71], 55 data points.
- T2K 14.93×10^{20} pot ν_e -appearance data [71], 23 data points for the CCQE and 16 data points for the CC1 π samples.
- T2K 11.24×10^{20} pot $\bar{\nu}_\mu$ -disappearance data [72], 55 data points.
- T2K 11.24×10^{20} pot $\bar{\nu}_e$ -appearance data [72], 23 data points.
- NO ν A 8.85×10^{20} pot ν_μ -disappearance data [45], 76 data points.
- NO ν A 8.85×10^{20} pot ν_e -appearance data [45], 13 data points.
- NO ν A 6.91×10^{20} pot $\bar{\nu}_\mu$ -disappearance data [45], 76 data points.
- NO ν A 6.91×10^{20} pot $\bar{\nu}_e$ -appearance data [45], 12 data points.

B Technical details and validation cross checks

This this appendix we provide some details on our analysis of the most recent data from accelerator and reactor experiments, and show that we can reproduce the results of the experimental collaborations with good accuracy, when using the same assumptions in the analysis.

B.1 T2K

The predicted number of events in the T2K far detector in a given energy bin i and for a given channel α can be calculated as

$$N_i^\alpha = N_{\text{bkg},i} + \int_{E_i}^{E_{i+1}} dE_{\text{rec}} \int_0^\infty dE_\nu R(E_{\text{rec}}, E_\nu) \frac{d\Phi}{dE_\nu} \sigma_\alpha(E_\nu) \varepsilon(E_\nu) P_{\nu_\mu \rightarrow \nu_\alpha}(E_\nu), \quad (\text{B.1})$$

where

- $N_{\text{bkg},i}$ is the number of background events in that bin, which we have extracted from Ref. [71] and consistently re-scaled to the latest exposure. If there is a neutrino component, its oscillation has to be consistently included.
- $[E_i, E_{i+1}]$ are the bin limits.
- E_{rec} is the reconstructed neutrino energy.
- E_ν is the true neutrino energy.
- $R(E_{\text{rec}}, E_\nu)$ is the energy reconstruction function, that we take to be Gaussian.
- $\frac{d\Phi}{dE_\nu}$ is the incident ν_μ flux, extracted from Ref. [73].
- σ_α is the ν_α detector cross-section, extracted from Ref. [73].
- ε is the detection efficiency, which is adjusted to reproduce the observed spectra in Ref. [72].
- $P_{\nu_\mu \rightarrow \nu_\alpha}(E_\nu)$ is the $\nu_\mu \rightarrow \nu_\alpha$ oscillation probability.

For the antineutrino channel, one has to switch ν by $\bar{\nu}$.

If we assume a Poissonian χ^2 with the data points in Ref. [72], add an overall normalisation systematic uncertainty⁵ and combine all the data, we get the contours in fig. 12. The other oscillation parameters are fixed as specified in Ref. [72] and the reactor uncertainty on θ_{13} is included as a Gaussian bias and marginalised over. Finally, following the ad-hoc procedure described in section 8.4.2 in Ref. [72], the disappearance Δm_{32}^2 contours are manually Gaussian-smearred with a standard deviation $\sigma = 4.1 \cdot 10^{-5} \text{ eV}^2$.

B.2 NOvA

For NOvA the predicted number of events is given, as for T2K, by Eq. (B.1). Fluxes and detector response are extracted from Refs. [74, 75]. We take the data points and backgrounds from Ref. [75] and with those construct a Poissonian χ^2 including an normalisation systematic uncertainty⁶ and we get the contours in fig. 13 when the undisplayed oscillation parameters are fixed as specified in Ref. [75]. In particular the reactor uncertainty on θ_{13} is included as a Gaussian bias and marginalised over.

⁵We take it to be 7% for the ν_μ and $\bar{\nu}_\mu$ disappearance channels, 5% for the $\bar{\nu}_e$ appearance channel, 8% for the CCQE ν_e appearance channel, and 23% for the CC1 π ν_e appearance channel.

⁶We take it to be 5% for ν_e appearance, 6% for $\bar{\nu}_e$ appearance, and 6% for both the ν_μ and $\bar{\nu}_\mu$ disappearance channels. We take these uncertainties as fully correlated for the disappearance channels.

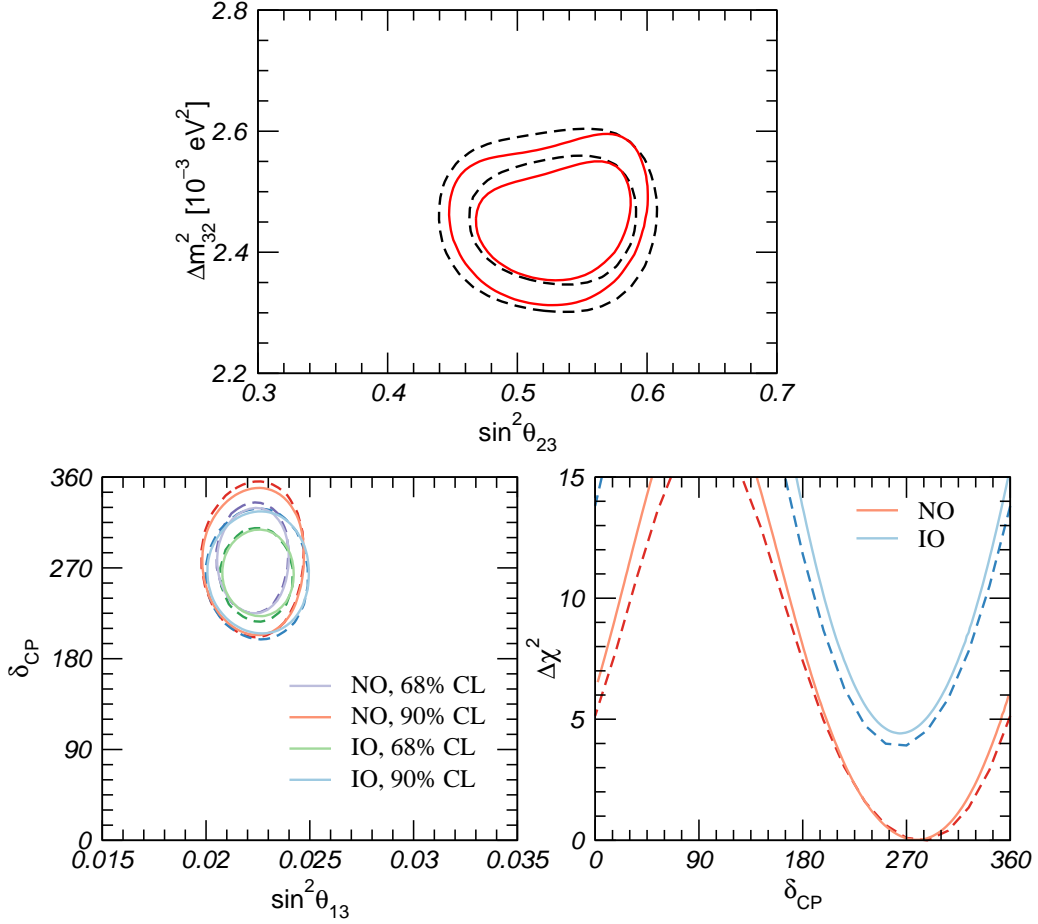


Figure 12. Different projections to our fit to latest T2K data (dashed lines) compared to the corresponding results of the experimental collaboration (solid curves), as presented in Ref. [72], when adopting the same assumptions. All unshown parameters are marginalised over.

B.3 Daya Bay

The Daya Bay 3ν oscillation analysis is based on [21], the data is taken from the supplementary material provided on arXiv.

In each experimental hall in Daya Bay there are more than one detector, so the number of events in hall H , N_i^H is a sum of the contributions in all the detectors in the hall. The predicted numbers of events in a detector d in an energy bin i is computed as

$$N_i^d = \mathcal{N} \sum_r \sum_{\text{iso}} \frac{\epsilon^d}{L_{rd}^2} \int_{E_i^{\text{rec}}}^{E_{i+1}^{\text{rec}}} dE^{\text{rec}} \int_0^\infty dE_\nu \sigma(E_\nu) f^{\text{iso}} \phi^{\text{iso}}(E_\nu) P_{\bar{\nu}_e \rightarrow \bar{\nu}_e}^{rd}(E_\nu) R(E^{\text{rec}}, E_\nu). \quad (\text{B.2})$$

The indices i , r , d , iso refer to the energy bin, reactor, detector, and fissible isotope, respectively. ϵ^d are the detector efficiencies, including $\epsilon_\mu \times \epsilon_m$ multiplied by the life time days (taken both from table I in [21]) as well as the relative difference of target protons ΔN_p in each detector, obtained from table VI in [76]. L_{rd} are the baselines between the reactor

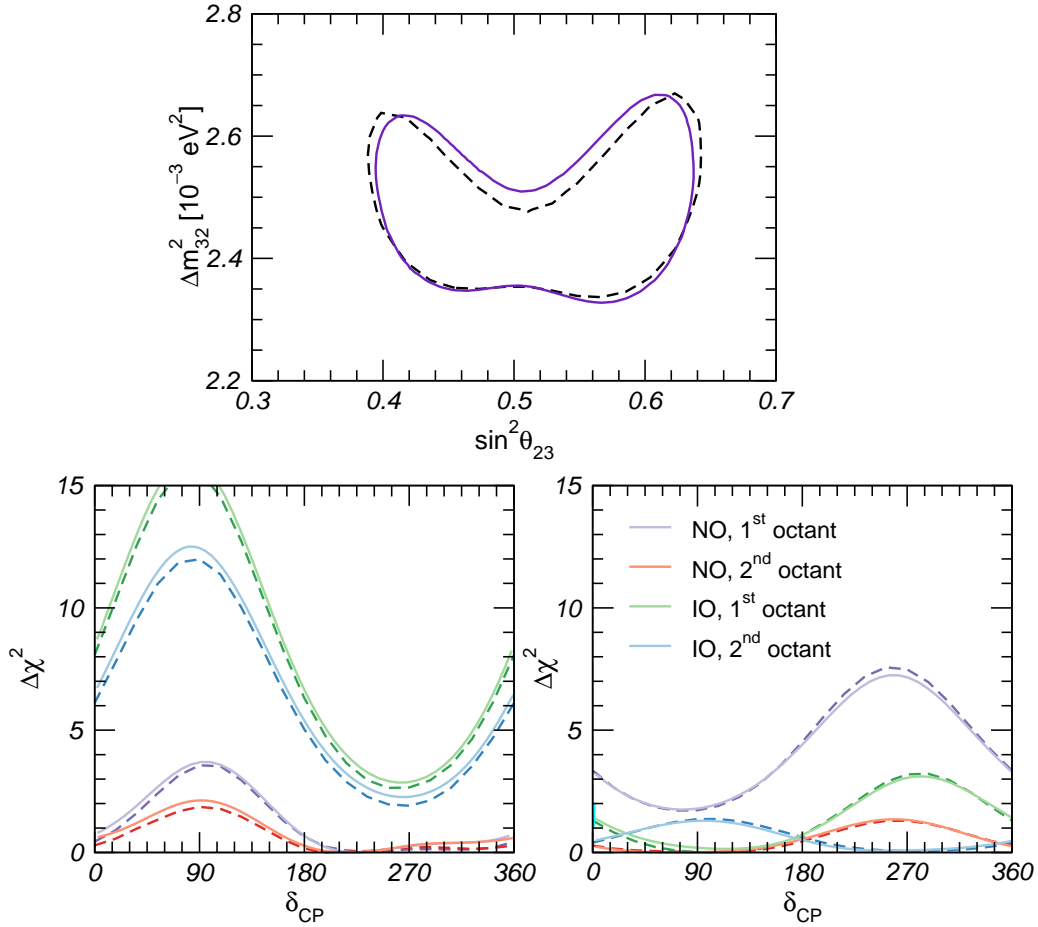


Figure 13. Different projections to our fit to latest NOvA data (dashed lines) compared to the corresponding results of the experimental collaboration (solid curves), as presented in Ref. [45], when adopting the same assumptions. The upper plot only includes disappearance data, whereas the bottom left plot corresponds to ν_e appearance and the bottom right plot to $\bar{\nu}_e$ appearance.

r and detector d , obtained from table I in [76]. E_ν and E^{rec} are the true and reconstructed neutrino energy, which are related by the detector response function $R(E^{\text{rec}}, E_{\text{prompt}})$, provided in the complementary material to [21]. The relation between the prompt energy E_{prompt} and the neutrino energy E_ν is $E_\nu = m_n - m_p - m_e + E_{\text{prompt}}$. $\sigma(E_\nu)$ is the Inverse Beta Decay cross section computed performing the integral over $\cos\theta$ of the differential cross section in [77]. $\phi^{\text{iso}}(E_\nu)$ are the Huber-Mueller flux predictions [78, 79] and f^{iso} are the fission fractions. For each isotope, f^{iso} is computed as the average of the fission fractions in table 9 of Ref. [25]. Following section 2.6 of [25], we apply non-equilibrium corrections by adding the relative correction from table VII of [79] to the fluxes [78, 79]. Since Daya Bay has run for a long period we take the row corresponding to 450 days. $P_{\bar{\nu}_e \rightarrow \bar{\nu}_e}^{rd}(E_\nu)$ is the oscillation probability. The global constant \mathcal{N} will cancel when taking ratios of event numbers.

Our DayaBay χ^2 is based on the ratios of the observed spectra in experimental halls 3 and 1 as well as 2 and 1:

$$\chi^2(\theta_{12}, \theta_{13}, \Delta m_{21}^2, \Delta m_{31}^2, \vec{\eta}) = \sum_i \frac{\left(\frac{O_i^3 - B_i^3(\vec{\eta})}{O_i^1 - B_i^1(\vec{\eta})} - \frac{N_i^3}{N_i^1}(\theta_{12}, \theta_{13}, \Delta m_{21}^2, \Delta m_{31}^2, \vec{\eta}) \right)^2}{(\sigma_i^{stat31})^2} + \sum_i \frac{\left(\frac{O_i^2 - B_i^2(\vec{\eta})}{O_i^1 - B_i^1(\vec{\eta})} - \frac{N_i^2}{N_i^1}(\theta_{12}, \theta_{13}, \Delta m_{21}^2, \Delta m_{31}^2, \vec{\eta}) \right)^2}{(\sigma_i^{stat21})^2} + \vec{\eta}^T V_\eta^{-1} \vec{\eta}. \quad (\text{B.3})$$

Here, O_i^H and $B_i^H(\vec{\eta})$ are the observed number of events and the background predictions in the experimental hall H and bin i , which can be found in the complementary material of [21]. $\sigma_i^{stat_{HH'}}$ are the errors of the ratio $[O_i^H - B_i^H(\vec{\eta})] / [O_i^{H'} - B_i^{H'}(\vec{\eta})]$, computed propagating the statistical errors of O_i^H and $O_i^{H'}$.⁷

In eq. (B.3), $\vec{\eta}$ is the vector of pull parameters and V_η is the pull correlation matrix which accounts for the systematic uncertainties and their correlations. In order to reproduce the Daya Bay results [21], systematics in detection efficiency, relative energy scale and cosmogenic Li-He background have to be taken into account. The detection efficiency and relative energy scale uncertainties are given by 0.13% and 0.2%, respectively [21, 76], and the Li-He background uncertainty is given by 30% [21]. We include also the uncertainties in accidental (1%) and fast neutron (13% (17%) in EH1 and EH2 (EH3)) backgrounds [76], which however play only a subleading role. We take into account the 5 systematics in each of the 3 experimental hall as uncorrelated, so V_η is a diagonal 15×15 matrix. In order to use the correct uncertainties in each experimental hall we divide the detector uncertainties by $\sqrt{2}$ in EH1 and EH2 and by $\sqrt{4}$ in EH3, since there are 2 and 4 detectors, respectively

In the left panel of fig. 14, our re-analysis is compared to the one published in [21].

B.4 RENO

The RENO 3ν oscillation analysis is based on [22]. The number of events in the near and far detectors are computed as in eq. (B.2), using the Daya Bay response function. The average fission fractions are taken from [80], the baselines from [81], and life time days can be found in [22]. In order to compute the total relative efficiency between the near and far detectors, a normalization to the total number of predicted events without oscillations in the far detector is performed. The RENO χ^2 is based on the far/near spectral ratio is implemented as follows:

$$\chi^2(\theta_{12}, \theta_{13}, \Delta m_{21}^2, \Delta m_{31}^2, \vec{\eta}) = \sum_i \frac{\left(\frac{O_i^F}{O_i^N} - \frac{N_i^F}{N_i^N}(\theta_{12}, \theta_{13}, \Delta m_{21}^2, \Delta m_{31}^2, \vec{\eta}) \right)^2}{(\sigma_i^{stat})^2} + \vec{\eta}^T V_\eta^{-1} \vec{\eta}. \quad (\text{B.4})$$

⁷We neglect the correlation of the statistical errors due to the events in EH1, which appear in both ratios. In this way we obtain better agreement with the results of the DayaBay collaboration, cf. fig. 14, indicating that this choice of errors provides a fair approximation.

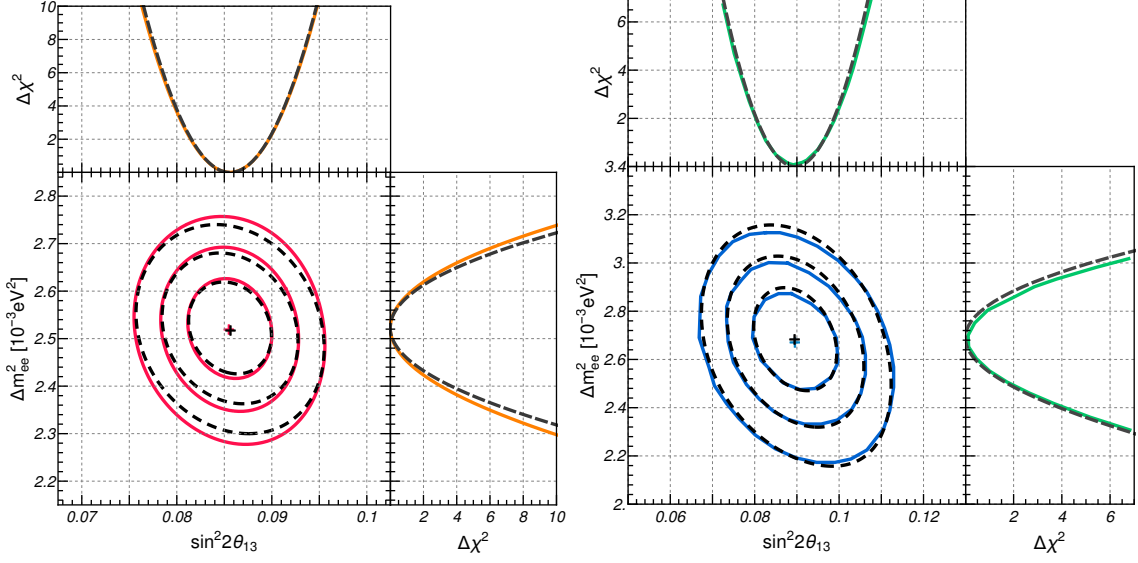


Figure 14. Our fit to DayaBay and RENO (black-dashed lines) compared to the results of the experimental collaborations (solid lines), as published in Refs. [21] and [22], respectively, when adopting the same assumptions. Following the collaborations, on the vertical axes, the parameter Δm_{ee}^2 defined in eq. (3.10) is used.

Here, $O_i^{F/N}$, are the observed number of events in the far and near detectors and energy bin i , with background expectations subtracted. The data is obtained from digitizing fig. 1 of [22]. $N_i^{F/N}$, are the corresponding predicted number of events, computed as in eq. (B.2) and σ_i^{stat} , are the statistical errors of the ratio $\frac{O_i^F}{O_i^N}$. $\vec{\eta}$ is the vector of the pull parameters and V_η is the pull correlation matrix which accounts for the systematic uncertainties associated to each pull parameter and their correlations.

Ref. [22] quotes systematic uncertainties in the relative detection efficiency and relative energy scale of 0.21% and 0.15%, respectively. The cosmogenic Li-He background plays no significant role, but is included as well with a relative uncertainty of 5% (8%) for the near (far) detector, cf. table I of [22]. In order to match precisely the results shown in fig. 3 of [22], an extra factor of 0.984 to the Far/Near ratio has to be included and the relative detection efficiency uncertainty has to be increased by a factor of 1.4. Our re-analysis of RENO data is compared to the official one in the right panel of fig. 14.

References

- [1] B. Pontecorvo, *Neutrino experiments and the question of leptonic-charge conservation*, *Sov. Phys. JETP* **26** (1968) 984–988.
- [2] V. N. Gribov and B. Pontecorvo, *Neutrino astronomy and lepton charge*, *Phys. Lett.* **B28** (1969) 493.
- [3] Z. Maki, M. Nakagawa and S. Sakata, *Remarks on the unified model of elementary particles*, *Prog. Theor. Phys.* **28** (1962) 870–880.

- [4] M. Kobayashi and T. Maskawa, *CP Violation in the Renormalizable Theory of Weak Interaction*, *Prog. Theor. Phys.* **49** (1973) 652–657.
- [5] N. Cabibbo, *Time Reversal Violation in Neutrino Oscillation*, *Phys. Lett.* **72B** (1978) 333–335.
- [6] S. M. Bilenky, J. Hosek and S. T. Petcov, *On Oscillations of Neutrinos with Dirac and Majorana Masses*, *Phys. Lett.* **B94** (1980) 495.
- [7] V. D. Barger, K. Whisnant and R. J. N. Phillips, *CP Violation in Three Neutrino Oscillations*, *Phys. Rev. Lett.* **45** (1980) 2084.
- [8] P. Langacker, S. T. Petcov, G. Steigman and S. Toshev, *On the Mikheev-Smirnov-Wolfenstein (MSW) Mechanism of Amplification of Neutrino Oscillations in Matter*, *Nucl. Phys.* **B282** (1987) 589.
- [9] M. C. Gonzalez-Garcia, M. Maltoni and T. Schwetz, *Updated Fit to Three Neutrino Mixing: Status of Leptonic CP Violation*, *JHEP* **11** (2014) 052, [[1409.5439](#)].
- [10] M. Gonzalez-Garcia, M. Maltoni, J. Salvado and T. Schwetz, *Global fit to three neutrino mixing: critical look at present precision*, *JHEP* **1212** (2012) 123, [[1209.3023](#)].
- [11] I. Esteban, M. C. Gonzalez-Garcia, M. Maltoni, I. Martínez-Soler and T. Schwetz, *Updated Fit to Three Neutrino Mixing: Exploring the Accelerator-Reactor Complementarity*, *JHEP* **01** (2017) 087, [[1611.01514](#)].
- [12] “NuFit webpage.” <http://www.nu-fit.org>.
- [13] P. F. de Salas, D. V. Forero, C. A. Ternes, M. Tortola and J. W. F. Valle, *Status of neutrino oscillations 2018: 3σ hint for normal mass ordering and improved CP sensitivity*, *Phys. Lett.* **B782** (2018) 633–640, [[1708.01186](#)].
- [14] F. Capozzi, E. Lisi, A. Marrone and A. Palazzo, *Current Unknowns in the Three Neutrino Framework*, *Prog. Part. Nucl. Phys.* **102** (2018) 48–72, [[1804.09678](#)].
- [15] MINOS collaboration, P. Adamson et al., *Measurement of Neutrino and Antineutrino Oscillations Using Beam and Atmospheric Data in MINOS*, *Phys. Rev. Lett.* **110** (2013) 251801, [[1304.6335](#)].
- [16] MINOS collaboration, P. Adamson et al., *Electron neutrino and antineutrino appearance in the full MINOS data sample*, *Phys. Rev. Lett.* (2013) , [[1301.4581](#)].
- [17] T2K collaboration, K. Abe et al., *Measurement of neutrino and antineutrino oscillations by the T2K experiment including a new additional sample of ν_e interactions at the far detector*, *Phys. Rev.* **D96** (2017) 092006, [[1707.01048](#)]. [Erratum: *Phys. Rev.*D98,no.1,019902(2018)].
- [18] T2K collaboration, K. Abe et al., *Search for CP violation in Neutrino and Antineutrino Oscillations by the T2K experiment with 2.2×10^{21} protons on target*, *Phys. Rev. Lett.* **121** (2018) 171802, [[1807.07891](#)].
- [19] NOvA collaboration, P. Adamson et al., *Constraints on Oscillation Parameters from ν_e Appearance and ν_μ Disappearance in NOvA*, *Phys. Rev. Lett.* **118** (2017) 231801, [[1703.03328](#)].
- [20] NOvA collaboration, M. A. Acero et al., *New constraints on oscillation parameters from ν_e appearance and ν_μ disappearance in the NOvA experiment*, *Phys. Rev.* **D98** (2018) 032012, [[1806.00096](#)].

- [21] DAYA BAY collaboration, D. Adey et al., *Measurement of Electron Antineutrino Oscillation with 1958 Days of Operation at Daya Bay*, [1809.02261](#).
- [22] RENO collaboration, G. Bak et al., *Measurement of Reactor Antineutrino Oscillation Amplitude and Frequency at Reno*, [1806.00248](#).
- [23] DOUBLE CHOOZ collaboration, Y. Abe et al., *Improved measurements of the neutrino mixing angle θ_{13} with the Double Chooz detector*, *JHEP* **10** (2014) 086, [[1406.7763](#)]. [Erratum: JHEP02,074(2015)].
- [24] M. Dentler, A. Hernandez-Cabezudo, J. Kopp, M. Maltoni and T. Schwetz, *Sterile neutrinos or flux uncertainties? Status of the reactor anti-neutrino anomaly*, *JHEP* **11** (2017) 099, [[1709.04294](#)].
- [25] DAYA BAY collaboration, F. P. An et al., *Improved Measurement of the Reactor Antineutrino Flux and Spectrum at Daya Bay*, *Chin. Phys.* **C41** (2017) 013002, [[1607.05378](#)].
- [26] BOREXINO collaboration, M. Agostini et al., *Comprehensive measurement of pp-chain solar neutrinos*, *Nature* **562** (2018) 505–510.
- [27] ICECUBE collaboration, M. Aartsen et al., *Determining neutrino oscillation parameters from atmospheric muon neutrino disappearance with three years of IceCube DeepCore data*, *Phys. Rev.* **D91** (2015) 072004, [[1410.7227](#)].
- [28] ICECUBE collaboration, J. P. Yanez et al., “IceCube Oscillations: 3 years muon neutrino disappearance data.” http://icecube.wisc.edu/science/data/nu_osc.
- [29] SUPER-KAMIOKANDE collaboration, K. Abe et al., *Atmospheric Neutrino Oscillation Analysis with External Constraints in Super-Kamiokande I-IV*, *Phys. Rev.* **D97** (2018) 072001, [[1710.09126](#)].
- [30] SUPERKAMIOKANDE collaboration, “Atmospheric neutrino oscillation analysis with external constraints in Super-Kamiokande I-IV.” link to data release: <http://www-sk.icrr.u-tokyo.ac.jp/sk/publications/result-e.html#atmossci2018>, 2018.
- [31] ICECUBE collaboration, M. G. Aartsen et al., *Measurement of Atmospheric Neutrino Oscillations at 656 GeV with IceCube DeepCore*, *Phys. Rev. Lett.* **120** (2018) 071801, [[1707.07081](#)].
- [32] J. Elevant and T. Schwetz, *On the determination of the leptonic CP phase*, *JHEP* **09** (2015) 016, [[1506.07685](#)].
- [33] M. C. Gonzalez-Garcia and C. Pena-Garay, *Three neutrino mixing after the first results from K2K and KamLAND*, *Phys. Rev.* **D68** (2003) 093003, [[hep-ph/0306001](#)].
- [34] C. Jarlskog, *Commutator of the Quark Mass Matrices in the Standard Electroweak Model and a Measure of Maximal CP Violation*, *Phys.Rev.Lett.* **55** (1985) 1039.
- [35] PARTICLE DATA GROUP collaboration, M. Tanabashi et al., *Review of particle physics*, *Phys. Rev. D* **98** (Aug, 2018) 030001.
- [36] J. Bergstrom, M. C. Gonzalez-Garcia, M. Maltoni, C. Pena-Garay, A. M. Serenelli and N. Song, *Updated determination of the solar neutrino fluxes from solar neutrino data*, *JHEP* **03** (2016) 132, [[1601.00972](#)].
- [37] N. Vinyoles, A. M. Serenelli, F. L. Villante, S. Basu, J. Bergstrm, M. C. Gonzalez-Garcia

- et al., *A new Generation of Standard Solar Models*, *Astrophys. J.* **835** (2017) 202, [[1611.09867](#)].
- [38] L. Wolfenstein, *Neutrino oscillations in matter*, *Phys. Rev.* **D17** (1978) 2369–2374.
- [39] S. P. Mikheev and A. Y. Smirnov, *Resonance enhancement of oscillations in matter and solar neutrino spectroscopy*, *Sov. J. Nucl. Phys.* **42** (1985) 913–917.
- [40] M. Ikeda, “Solar neutrino measurements with Super-Kamiokande.” Talk given at the *XXVIII International Conference on Neutrino Physics and Astrophysics*, Heidelberg, Germany, June 4–9, 2018.
- [41] Y. Nakano, *^8B solar neutrino spectrum measurement using Super-Kamiokande IV*. PhD thesis, Tokyo U., 2016-02.
- [42] N. Okamura, *Effect of the Smaller Mass-Squared Difference for the Long Base-Line Neutrino Experiments*, *Prog. Theor. Phys.* **114** (2006) 1045–1056, [[hep-ph/0411388](#)].
- [43] H. Nunokawa, S. J. Parke and R. Zukanovich Funchal, *Another Possible Way to Determine the Neutrino Mass Hierarchy*, *Phys. Rev.* **D72** (2005) 013009, [[hep-ph/0503283](#)].
- [44] M. Wascko, *T2k status, results, and plans*, June, 2018. <https://doi.org/10.5281/zenodo.1286752>, 10.5281/zenodo.1286752.
- [45] M. Sanchez, *Nova results and prospects*, June, 2018. <https://doi.org/10.5281/zenodo.1286758>, 10.5281/zenodo.1286758.
- [46] V. D. Barger, K. Whisnant, S. Pakvasa and R. Phillips, *Matter Effects on Three-Neutrino Oscillations*, *Phys.Rev.* **D22** (1980) 2718.
- [47] H. Minakata, H. Nunokawa, S. J. Parke and R. Zukanovich Funchal, *Determining Neutrino Mass Hierarchy by Precision Measurements in Electron and Muon Neutrino Disappearance Experiments*, *Phys. Rev.* **D74** (2006) 053008, [[hep-ph/0607284](#)].
- [48] M. Blennow and T. Schwetz, *Determination of the Neutrino Mass Ordering by Combining Pingu and Daya Bay II*, *JHEP* **09** (2013) 089, [[1306.3988](#)].
- [49] ICECUBE collaboration, “Measurement of atmospheric neutrino oscillations with three years of data from the full sky.” <https://icecube.wisc.edu/science/data/2018nuosc>, 2018.
- [50] F. Halzen Talk given at the *History of the Neutrino Conference*, Paris, France, September 5–7, 2018, 2018.
- [51] J. Bonn et al., *The Mainz neutrino mass experiment*, *Nucl. Phys. Proc. Suppl.* **91** (2001) 273–279. [[PoSHeP2001,192\(2001\)](#)].
- [52] KATRIN collaboration, A. Osipowicz et al., *Katrin: a Next Generation Tritium Beta Decay Experiment with Sub-Ev Sensitivity for the Electron Neutrino Mass. Letter of Intent*, [hep-ex/0109033](#).
- [53] GERDA collaboration, M. Agostini et al., *Improved Limit on Neutrinoless Double- β Decay of ^{76}Ge from GERDA Phase II*, *Phys. Rev. Lett.* **120** (2018) 132503, [[1803.11100](#)].
- [54] KAMLAND-ZEN collaboration, A. Gando et al., *Search for Majorana Neutrinos near the Inverted Mass Hierarchy Region with KamLAND-Zen*, *Phys. Rev. Lett.* **117** (2016) 082503, [[1605.02889](#)]. [Addendum: *Phys. Rev. Lett.*117,no.10,109903(2016)].
- [55] J. J. Gomez-Cadenas, J. Martin-Albo, M. Mezzetto, F. Monrabal and M. Sorel, *The Search for neutrinoless double beta decay*, *Riv. Nuovo Cim.* **35** (2012) 29–98, [[1109.5515](#)].

- [56] G. L. Fogli, E. Lisi, A. Marrone, A. Melchiorri, A. Palazzo, P. Serra et al., *Observables sensitive to absolute neutrino masses: Constraints and correlations from world neutrino data*, *Phys. Rev.* **D70** (2004) 113003, [[hep-ph/0408045](#)].
- [57] S. Pascoli, S. T. Petcov and T. Schwetz, *The Absolute Neutrino Mass Scale, Neutrino Mass Spectrum, Majorana C_p -Violation and Neutrinoless Double-Beta Decay*, *Nucl. Phys.* **B734** (2006) 24–49, [[hep-ph/0505226](#)].
- [58] B. T. Cleveland et al., *Measurement of the solar electron neutrino flux with the Homestake chlorine detector*, *Astrophys. J.* **496** (1998) 505–526.
- [59] F. Kaether, W. Hampel, G. Heusser, J. Kiko and T. Kirsten, *Reanalysis of the GALLEX solar neutrino flux and source experiments*, *Phys. Lett.* **B685** (2010) 47–54, [[1001.2731](#)].
- [60] SAGE collaboration, J. N. Abdurashitov et al., *Measurement of the solar neutrino capture rate with gallium metal. III: Results for the 2002–2007 data-taking period*, *Phys. Rev.* **C80** (2009) 015807, [[0901.2200](#)].
- [61] SUPER-KAMIOKANDE collaboration, J. Hosaka et al., *Solar neutrino measurements in Super-Kamiokande-I*, *Phys. Rev.* **D73** (2006) 112001, [[hep-ex/0508053](#)].
- [62] SUPER-KAMIOKANDE collaboration, J. Cravens et al., *Solar neutrino measurements in Super-Kamiokande-II*, *Phys. Rev.* **D78** (2008) 032002, [[0803.4312](#)].
- [63] SUPER-KAMIOKANDE collaboration, K. Abe et al., *Solar neutrino results in Super-Kamiokande-III*, *Phys. Rev.* **D83** (2011) 052010, [[1010.0118](#)].
- [64] SNO collaboration, B. Aharmim et al., *Combined Analysis of All Three Phases of Solar Neutrino Data from the Sudbury Neutrino Observatory*, *Phys. Rev.* **C88** (2013) 025501, [[1109.0763](#)].
- [65] BOREXINO collaboration, G. Bellini et al., *Precision measurement of the ^7Be solar neutrino interaction rate in Borexino*, *Phys. Rev. Lett.* **107** (2011) 141302, [[1104.1816](#)].
- [66] BOREXINO collaboration, G. Bellini et al., *Measurement of the solar ^8B neutrino rate with a liquid scintillator target and 3 MeV energy threshold in the Borexino detector*, *Phys. Rev.* **D82** (2010) 033006, [[0808.2868](#)].
- [67] BOREXINO collaboration, G. Bellini et al., *Neutrinos from the primary protonproton fusion process in the Sun*, *Nature* **512** (2014) 383–386.
- [68] M. Honda, M. Sajjad Athar, T. Kajita, K. Kasahara and S. Midorikawa, *Atmospheric Neutrino Flux Calculation Using the Nrlmsise-00 Atmospheric Model*, *Phys. Rev.* **D92** (2015) 023004, [[1502.03916](#)].
- [69] KAMLAND collaboration, A. Gando et al., *Reactor On-Off Antineutrino Measurement with Kamland*, *Phys. Rev.* **D88** (2013) 033001, [[1303.4667](#)].
- [70] A. Cabrera Serra, “Double Chooz Improved Multi-Detector Measurements.” Talk given at the *CERN EP colloquium*, CERN, Switzerland, September 20, 2016.
- [71] A. Izmaylov, “T2K Neutrino Experiment. Recent Results and Plans.” Talk given at the *Flavour Physics Conference*, Quy Nhon, Vietnam, August 13–19, 2017.
- [72] T. Koga, *Measurement of neutrino interactions on water and search for electron anti-neutrino appearance in the T2K experiment*. PhD thesis, Tokyo U., 2018-07. <https://www.t2k.org/docs/thesis/090/Doctor%20thesis>.

- [73] S. Dennis, *Muon Antineutrino Disappearance and Non-Standard Interactions at the T2K Experiment*. PhD thesis, Warwick U., 2015-10-24.
- [74] M. BAIRD, *Reconstructing Neutrino Energies with the NOvA Detectors*, June, 2018. [10.5281/zenodo.1301120](https://zenodo.org/record/1301120).
- [75] A. Himmel, “First Oscillation Results with Neutrino and Antineutrino Beams in NOvA.” Talk given at the *Joint Theoretical-Experimental Physics Seminar*, Fermilab, USA, June 15, 2018.
- [76] DAYA BAY collaboration, F. P. An et al., *Measurement of electron antineutrino oscillation based on 1230days of operation of the Daya Bay experiment*, *Phys. Rev.* **D95** (2017) 072006, [[1610.04802](https://arxiv.org/abs/1610.04802)].
- [77] P. Vogel and J. F. Beacom, *Angular Distribution of Neutron Inverse Beta Decay, $\bar{\nu}_e + p \rightarrow e^+ + n$* , *Phys. Rev.* **D60** (1999) 053003, [[hep-ph/9903554](https://arxiv.org/abs/hep-ph/9903554)].
- [78] P. Huber, *On the determination of anti-neutrino spectra from nuclear reactors*, *Phys.Rev.* **C84** (2011) 024617, [[1106.0687](https://arxiv.org/abs/1106.0687)].
- [79] T. Mueller, D. Lhuillier, M. Fallot, A. Letourneau, S. Cormon et al., *Improved Predictions of Reactor Antineutrino Spectra*, *Phys.Rev.* **C83** (2011) 054615, [[1101.2663](https://arxiv.org/abs/1101.2663)].
- [80] RENO collaboration, G. Bak et al., *Fuel-Composition Dependent Reactor Antineutrino Yield and Spectrum at Reno*, [1806.00574](https://arxiv.org/abs/1806.00574).
- [81] RENO collaboration, J. K. Ahn et al., *RENO: An Experiment for Neutrino Oscillation Parameter θ_{13} Using Reactor Neutrinos at Yonggwang*, [1003.1391](https://arxiv.org/abs/1003.1391).